



Review Article

Muon tomography in geoscientific research – A guide to best practice



Alessandro Lechmann^{a,*}, David Mair^a, Akitaka Ariga^{b,1}, Tomoko Ariga^c, Antonio Ereditato^b,
 Ryuichi Nishiyama^{b,2}, Ciro Pistillo^b, Paola Scampoli^{b,d}, Fritz Schlunegger^a,
 Mykhailo Vladymyrov^{b,3}

^a Institute of Geological Sciences, University of Bern, Bern CH-3012, Switzerland

^b Albert Einstein Center for Fundamental Physics, Laboratory for High Energy Physics, University of Bern, Bern CH-3012, Switzerland

^c Faculty of Arts and Science, Kyushu University, Fukuoka J-812-8582, Japan

^d Dipartimento di Fisica "E.Pancini", Università di Napoli Federico II, Napoli I-80126, Italy

ARTICLE INFO

Keywords:

Muon tomography
 Muography
 Muon radiography
 Geophysics
 Particle physics

ABSTRACT

The use of muon tomography in geoscience projects has been continuously increasing over the past few years. This led to a variety of applications that often use custom-tailored solutions for data acquisition and processing. The respective know-how is splintered and mainly available in a semi-published state in various physics departments that developed these methods. This complicates the design of new studies and the decision whether muon tomography is a suitable tool and feasible for a specific geoscientific question. In this study we review the current state of how muon tomography has been applied in the field of geosciences with the goal of equipping interested geoscientists with the basic knowledge on the physical basics that constitute muon tomography. After an explanation of how muons are produced, how they traverse matter and how they are recorded, a showcase is made of recent applications. These studies show the variety of how muon tomography can be applied in experiments, such that interested readers may implement this technology for their own research. Finally, we provide a guide to best practice to help interested geoscientists decide if and how muon tomography could be implemented in their own research. We believe that through a better mutual understanding, new interdisciplinary collaborations can be initiated that advance the whole field of muon tomography.

1. Introduction

1.1. General introduction

Many industrial and scientific problems dealing with geological matters require some form of geophysical exploration, or remote sensing in the broader sense. Often detailed knowledge of the local geology, i.e. lithological structures in the surroundings, is needed as an integral part of most surveys. The field of geophysics offers a rather large variety of well-established methods to meet this need. Depending on the exact nature of information that has to be gathered and the deployment constraints in the field, one is usually free to choose between seismological (sensitive to density), gravimetric (also sensitive to density), and

electromagnetic (like ground penetrating radar or electrical resistivity tomography; both sensitive to electrical resistivity) methods (e.g. [Kearey et al., 2002](#)).

A large amount of scientific work in geophysics is dedicated to the refinement of existing techniques, e.g. by deploying advanced mathematical and computational models supported by powerful computers (e.g. [Reichstein et al., 2019](#)) improving workflows for the data analysis, optimising the experimental setups (e.g. [Maurer et al., 2010](#)), etc., such that these methods may be applied to new fields or even to extensive data sets that could not be handled before. It is thus rare to see a new technology emerge next to the continuously improving, yet already established geophysical methods. Nevertheless, since the start of the millennium naturally occurring cosmic rays – they are already exploited

* Corresponding author.

E-mail addresses: alessandro.lechmann@geo.unibe.ch (A. Lechmann), david.mair@geo.unibe.ch (D. Mair), akitaka.ariga@lhev.unibe.ch (A. Ariga), tomoko.ariga@cern.ch (T. Ariga), antonio.ereditato@cern.ch (A. Ereditato), r-nishi@eri.u-tokyo.ac.jp (R. Nishiyama), ciro.pistillo@cern.ch (C. Pistillo), paola.scampoli@lhev.unibe.ch (P. Scampoli), fritz.schlunegger@geo.unibe.ch (F. Schlunegger), mykhailo.vladymyrov@tki.unibe.ch (M. Vladymyrov).

¹ Present address: Chiba University, Japan.

² Present address: Earthquake Research Institute, The University of Tokyo, Japan.

³ Present address: Theodor Kocher Institute, University of Bern, Switzerland.

<https://doi.org/10.1016/j.earscrev.2021.103842>

Received 15 July 2021; Received in revised form 20 September 2021; Accepted 13 October 2021

Available online 18 October 2021

0012-8252/© 2021 The Authors. Published by Elsevier B.V. This is an open access article under the CC BY license (<http://creativecommons.org/licenses/by/4.0/>).

by the geochronology community for dating purposes – have increasingly been utilised to gain insights on geological matters (see Ch. 3 for an overview). As only the muonic part of the cosmic ray spectrum is used, this novel research field has been given the name of “muon tomography” (see Ch. 2.1 for nomenclature, as also other notions are commonly used). Tanaka and Oláh (2019) show how the number of studies employing this new technology has been continuously growing.

Nowadays the technology has advanced beyond a pure proof-of-concept state, such that it may be applied as a central part of geological/geophysical research. Even though a few companies have begun to develop muon detectors at an industrial level (e.g. Harel and Yaish, 2019), the vast majority of detector design and construction is still very much concentrated at the universities. This entails that the detector know-how is splintered across the physics departments where particle detectors have been developed over the past years (e.g. Ariga et al., 2018). Generally speaking, muon tomography is used to reconstruct the geometry of an internal structure of a (geological) body of interest that is penetrated by muons. The muon flux is attenuated upon penetrating the target body, and the muons are registered on a detector. Fig. 1 shows a possible setup with a glacier, a rock column underneath this glacier, and a detector within a tunnel. Applications of muon tomography for the purpose of mapping the ice-bedrock interface thus need the knowledge on the physics of muons and on the muon flux model. Additionally, an understanding is required of how such a flux is attenuated upon traversing matter, and how a detector registering the muons is built. Finally, applications of muon tomography also base on mathematical tools that are used to invert the registered muon flux into a geometric model for the traversed matter of interest (Fig. 1).

This is the starting point of the present work as we see much potential for the further development of muon tomography with a large field of applications in geoscience research. We consider that a broader understanding of this technique would enable earth scientists to shape the

direction of future muon tomography research. Once geoscientists are able to clearly state their needs, while knowing the capabilities and limitations of this technique, particle physicists may be encouraged to develop their detectors accordingly. This paper addresses primarily geoscientists who have few to none experience with muon tomography. The scope of this review article is to equip them with the necessary information to approach a physics group for potential collaborations. We aim at providing a broad overview of how this technology works and setting the important geophysical equations in the related context, thereby considering different settings and questions, and we develop a guide that serves to facilitate decisions along with guidelines of how to proceed.

Accordingly, we first introduce in Ch. 1.2 the particle physical context from which this technology historically emerged. Chapter 2 explains central technical elements of muon tomography. This starts with a thorough description of the various muon flux models that can be utilised. The chapter continues with an explanation of the energy loss equation and possible ways to solve it. It is followed by an overview on the various detector types, their advantages, and drawbacks. The chapter then concludes with a brief description of various methods to tackle the whole data analysis aspect in order to provide the user with a few starting points for their own research. Chapter 3 provides the reader with a showcase of muon tomographic studies that were employed in a geoscientific setting. This is supposed to give the prospective users an overview of the range of possible applications of this technology. Chapter 4 outlines the most important steps that a geoscientist interested in using muon tomography for their project needs to consider.

1.2. A short history of muon tomography

The story of how muon tomography has evolved has to be taken as far back as to the first measurements of cosmic rays on the Eiffel tower

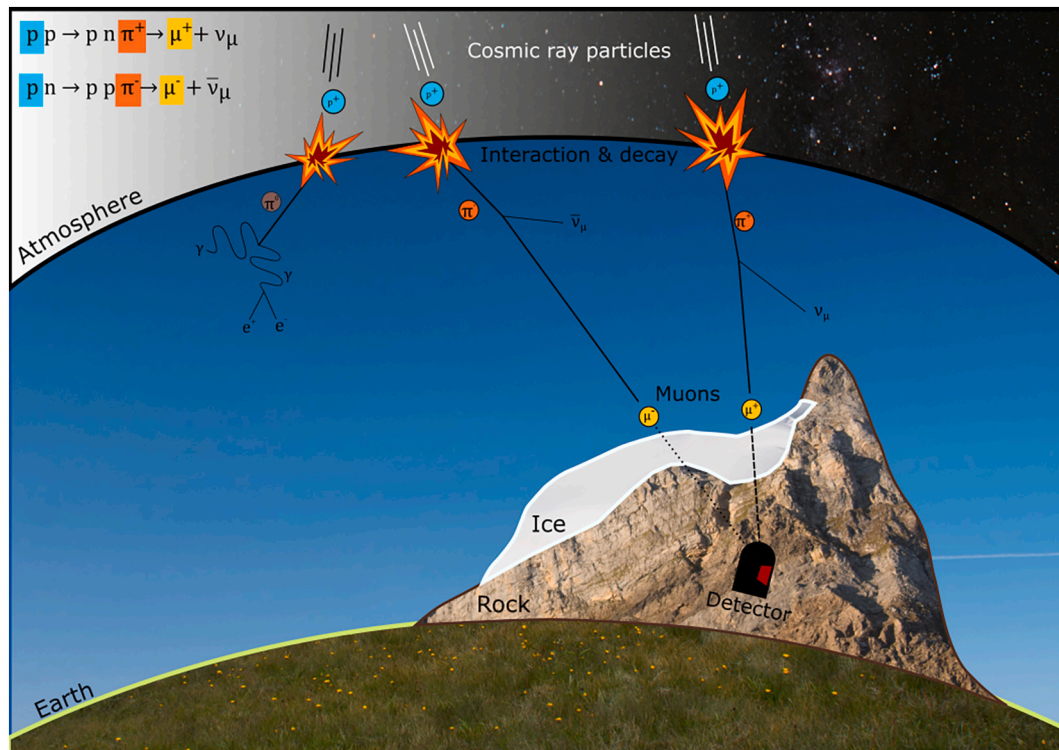


Fig. 1. Sketch illustrating the components that are involved in an experiment where muon tomography is used. Commonly, the objects to be analysed comprise solid matter with density contrasts (here the boundary between a glacier and bedrock). A detector registers the muons that traverse both the glacier and the underlying bedrock. Muon tomography exploits the fact that the muon flux along the dashed trajectory is higher due to the lower average density of the material. The dotted trajectory on the other hand features a higher average density and hence less muons pass from that direction. Through inversion, it is possible to use the pattern of registered muons from multiple directions as basis to reconstruct the geometry of the glacier's base.

(Wulf, 1910), underwater (Pacini, 1912) and during balloon flights (Hess, 1912) at the onset of the 20th century. These important experiments marked the beginning of numerous discoveries that were to come and eventually established the field of particle physics. Aided by the parallel advances in quantum mechanics, many new subatomic particles were found, most notably the proton (Bohr, 1913; Rutherford, 1919), the neutron (Chadwick, 1932), the positron (Anderson, 1932) and the muon (Neddermeyer and Anderson, 1937). Naturally occurring particles from the aforementioned cosmic ray flux were the most important source to experimentally study particles, their interactions, and decays. This has been the state of research even long before the gargantuan particle accelerators were built.

The circumstance that electrically charged particles lose energy and/or change momentum when they penetrate any kind of material was already known at this time, as the experiments by Rutherford (1911) show. This model of energy loss is still used today as a backbone for particle tomographic applications and has been refined since the early 20th century through meticulous experiments. The reader is referred to Tanabashi et al. (2018) for an overview of all the intricacies that are involved in the energy loss calculations as well as to Groom et al. (2001) for the case of muons.

These early discoveries have sparked the interest of numerous researchers to utilise cosmic rays to gain insight into a body placed between the source of cosmic rays and a particle detector. This was first done by George (1955) for the calculation of the overburden of a tunnel (similar to Fig. 1), which can be viewed as the first application of a tomographic setup where cosmic rays were used as the primary signal source. 15 years later Alvarez et al. (1970) set another milestone for this technology as they examined the famous pyramids at Giza, Egypt, for presumed hidden chambers. However, as the detector technology as well as the physical theories of energy loss were not that advanced at this stage, and thus the quality of the results was not good enough for any further examination, following-up studies have not been undertaken for about 20 years.

The development of the detector technology took a significant step forward with the establishment of numerous underground laboratories and the subsequent onset of large-scale experiments in particle physics. Bettini (2014b) presents an overview of different underground laboratories around the world. Among these are the Gran Sasso National Laboratory in Abruzzo in Central Italy and the Kamioka Underground Observatory in Gifu prefecture in Central Japan that hosted the milestone neutrino oscillation experiment OPERA (Acquafredda et al., 2009) and the nucleon decay experiment KamiokaNDE (e.g. Kajita et al., 2012), respectively. The progress in detector technology was possible because physicists had to filter out noise induced by the naturally occurring cosmic rays that were interfering with their measurements. Underground laboratories provide a natural “shielding” against a large part of the cosmic ray particles that perpetually hit the Earth from above. The soil/rock overburden thus functions like a lead coat during an X-ray examination at the medical doctor, as this shield hinders particles to penetrate regions where they are undesired either for medical or technical reasons. Even though a significant part of the cosmic ray spectrum can be filtered out by performing an experiment in an underground laboratory, there exists still a component that may penetrate matter up to several kilometres and thus can be identified, measured, and analysed. These are the so-called muons. This is one of the peculiar cases where geoscientists (especially those working in cosmogenic nuclide dating, e.g. Gosse and Phillips, 2001) and particle physicists are confronted with the very same problem, when they are trying to quantify the muonic component in their measurements.

Without relying too much on particle physics theory (see reference below), these muons may be considered a “heavy version” of the electron, featuring a roughly 207-times higher mass. For more information on the physics of muons and how they were discovered, the reader is referred to the textbook by Bettini (2014a, p. 64-66). The mass difference between muons and electrons is the main reason why a muon of

equal velocity penetrates more matter than its electron counterpart, which incidentally also occurs in the cosmic ray particle flux.

Particle detectors have continuously been improved due to the ever-growing requirements for a better precision during new experiments. In parallel, the theory of how charged particles lose energy while travelling through matter has been largely improved by dedicated absorption experiments (see Groom et al., 2001, and references therein). The advances in these two areas were the prerequisites for further tomographic applications of cosmic rays (or more precisely cosmogenic muons). First attempts were made during the 90ies to characterise the internal structure of volcanoes in Japan (Nagamine, 1995; Nagamine et al., 1995). But only after the turn of the millennium the number of muon tomographic experiments started to increase. It was again the same Japanese research group from the Earthquake Research Institute in Tokyo (e.g. Tanaka et al., 2001, 2003, 2005) that pushed this new technology to a point where it can be considered as another valid method in the geophysical arsenal.

In recent years, several studies reviewed some technical aspects or the applications to specific sub-fields. Lesparre et al. (2010) provide a succinct overview of the technical basis of muon flux measurements, including a thorough review of time-dependent effects that might influence the quality of the results. They also discuss extensively different existing muon flux models. Although the subject is rather technical, the reader is referred to Groom et al. (2001) for a showcase of the central equations that govern the energy loss of muons traversing matter. Please note that the latter article does not focus on muon tomography in particular but presents the physical equations, which are valid for all muons. We would also like to point out a study by Kaiser (2019) that takes a rather unconventional standpoint. He explores the technology from an economic point of view and shows different directions in which this technology might evolve in the future. Marteau et al. (2012) present an earlier review that focuses mainly on volcanological applications and Procureur (2018) strongly focuses on scattering tomographic applications. Athanassas (2020) focuses in his work on how muon tomography may be applied in the context of hazard assessment (mostly in volcanic environments).

A very detailed review on muon tomography as a whole is given by Bonechi et al. (2020). Readers will find this review to be quite complementary to this work. While we focus on compiling the most important equations, Bonechi et al. (2020) provide a resourceful overview on detectors, applications, and common problems.

2. Principles of muon tomography

This section aims at introducing the corner posts of this technology. After a start where we explain of how this technology has been referred to in the literature, we progress to an explanation of the basic equations, namely the energy loss equation and the mathematical description of the cosmic ray flux. We complement this section with an overview of the main inversion techniques. In a subsequent section, the reader is introduced to the most important types of detectors (see also Fig. 1 for the components of a muon tomography experiment).

In this chapter, we proceed by following the path of a muon from its origin high in the stratosphere, to the matter it traverses, and finally to the detector where it will be recorded. We find this the simplest way to describe the cascade of processes that are involved in the passage of muons from their origins to the site where they are registered.

2.1. Terminology

As already mentioned in the introduction, there exist different terms that describe this technology, that vary from one research group to another. Here, we summarise the most common notions. We begin with a rather rare term, “muon radiography”. Radiography is usually an imaging technology where absorbing qualities of an object are rendered visible by exposing them to a form of radiation. A typical example of this

method is the X-ray image at a medical doctor's or dentist's office, where photons in the wavelength band between ca. 10 nm to 10 pm are used. The photographic films used in these applications are usually not directly sensitive to the photons directly, but to the electrons which are produced by the interaction of the photons with the atoms in the film. Consequently, such a radiography may be produced by any charged particle (muons in our case) that can be recorded.

A second, widely used term is “muon tomography”. Incidentally, this is also the notion that we use throughout this work. This selection bases on our own background in geophysics, where the term “tomography” is more widely spread (i.e. seismic tomography, electric resistivity tomography) than “radiography”. Apart from being used by different communities one may also define a technical distinction between “radiography” and “tomography”. Whereas the former describes a single transmission image at one point, the latter can then be referring to a 3D reconstruction of the interior density distribution. This corresponds very much to the difference between X-ray images (i.e. radiography) and a CT-scan (i.e. tomography) in medical applications.

A third notion, which recently has gained some interest in the community, is “muography”. This circumvents any historically grown connotations as this fictional word composition just means “draw/write with muons”.

Until the community agrees to use a “standard” description, one may take a pragmatic approach to this issue and use the 3 terms above interchangeably. However, as the practitioner in muon tomography inevitably has to research literature at some point, it is useful to be aware of all different notions that describe this technology.

2.2. The cosmic ray flux

This chapter aims at providing the reader with an overview on the different muon flux models that are currently available. This is done by introducing first the mechanisms that produce the muons in the first place. Afterwards, we present the reader with four selected muon flux models and show how they are parametrised. This includes a specification of how these models account for various parameters, such as height, incidence direction, etc. We close this section with a crude analysis of the uncertainty that is attached to these muon flux models and with recommendations for novice users.

2.2.1. Muon generation from primary cosmic rays

The starting point in our description of muon tomography is the site where the muons originate, i.e. the upper part of the atmosphere. In fact, muons are considered to be only “secondary” cosmic rays, as they are

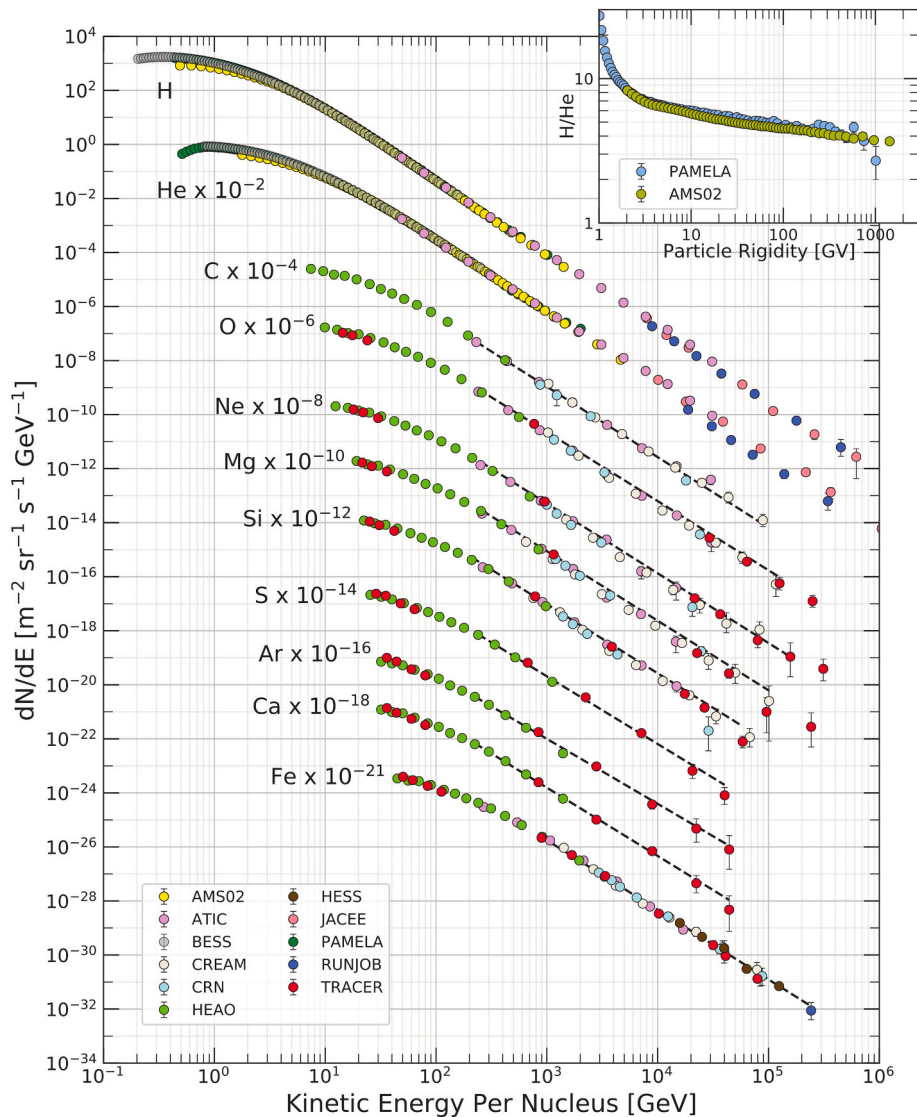


Fig. 2. Differential energy spectrum of primary cosmic ray particles, from Tanabashi et al. (2018, p. 424). Coloured markers denote different experiments. Please refer to Tanabashi et al. (2018, p. 424ff.) and references therein for further information.

only produced by interactions of so called “primary” cosmic rays with the atoms in our atmosphere. These primary cosmic rays have different origins. Whereas the largest part of the particles originates within our own galaxy and the sun, there is also a small fraction (although consisting of much higher velocity particles) that are of an intergalactic nature. A thorough description of the incident primary particle spectra can be found in the chapter “Cosmic Rays” in [Tanabashi et al. \(2018, p. 424ff.\)](#).

[Fig. 2](#) (Fig. 29.1 from [Tanabashi et al., 2018, p. 424](#)) shows the incident fluxes of different types of primary cosmic ray particles on a logarithmic plot. Strikingly, the most abundant particles to hit the atmosphere are hydrogen nuclei, i.e. protons, followed by helium atoms. Whereas the initial hydrogen to helium nuclei ratio is around 1000 at low energies, this difference seems to shrink towards higher energies, as can be verified by the inset of [Fig. 2](#). Other heavier nuclei do also hit the upper atmosphere; however, their contributions are negligible compared to hydrogen (and helium).

When these primary particles hit an atom in the upper atmosphere, new particles may be created (similar to collision experiments in particle accelerators). There are a large number of different interactions that might occur during these collisions. For a comprehensive overview, the reader is referred to [Gosse and Phillips \(2001, p. 1485ff.\)](#). Although this is a standard paper in the cosmogenic nuclide geochemistry community, we can make use of the same physical principles when we describe the cosmic ray flux (primary and secondary). As only a small portion of the overall interactions generate muons, we recreated a simplified version of [Fig. 1](#) of [Gosse and Phillips \(2001, p. 1486\)](#) below (see [Fig. 3](#)).

The incident primary cosmic ray particle (denoted with “pr” in [Fig. 3](#)) interacts with atoms and molecules in the upper atmosphere (the black circles, ●, in [Fig. 3](#)) and produces so-called “mesons” (e.g. [Gaisser et al., 2016](#)). These are elementary particles that consist of only two quarks compared to the three quarks in protons and neutrons (which are part of another group, the “baryons”). The important mesons for muon tomography are the pions (π^-, π^+) and the kaons (K^-, K^+). Readers interested in additional information on these particles are referred to a standard particle physics textbook (e.g. [Bettini, 2014a](#)). Pions as shown in [Fig. 3](#) decay in 99.99% of the cases ([Tanabashi et al., 2018, p. 1069 f.](#)) in the following form:



The products of such decays are a muon (μ^-, μ^+) and a neutrino, ν_μ (or antineutrino, $\bar{\nu}_\mu$). Neutrinos are weakly interacting particles, which are often formed during decays of particles and as a by-product of various radioactive decays. They are currently a very intensively studied branch of particle physics where considerable progress is being made. The award of the Nobel Prize in Physics to Takaaki Kajita and Arthur B. McDonald for their contributions to research in neutrino oscillations illustrates the importance of this development. Incidentally, this part of physics is another example of a fruitful collaboration between physicists and geoscientists, as in recent years they began to examine the generation of Earth’s heat by radioactive elements (potassium, uranium and thorium). The emitted neutrinos during the radioactive decay of the aforementioned elements allow inferences on their abundances (see for example [Šrámek et al., 2013](#) or [McDonough et al., 2020](#)).

The second kind of mesons, the kaons, have experienced a more complicated cascade of decays. In general, we are safe to consider that about two thirds, i.e. $\sim 67\%$ of the kaons directly decay to muons,



where one of the two channels produces also a neutral pion (i.e. without electric charge; this is however only a by-product and has no influence on any subsequent muons). Another $\sim 28\%$ of the kaons decay first into pions, which in turn decay according to the channels described above. As there are too many channels for presenting them in a simple list, we resort to a schematic notation:



The rest of the kaons decay into particles (mostly electrons) that are of no particular interest to muon tomographers. For a detailed list of the kaon decay channels please refer to [Tanabashi et al. \(2018, p. 1188 f.\)](#).

Once we know how the incoming muons are created, it is possible to develop cosmic ray flux models that describe the muon particle flux at a given location, which is defined by height above sea level, latitude and longitude, and a given incidence angle, i.e. any oblique angle with respect to the zenith (straight above).

Different researchers came up with various ways of how to describe this flux of cosmic ray muons mathematically. In this work we present 4 commonly encountered muon flux models. We additionally show a reasonable model error for the muon flux, which in turn may be used in any further computation.

Generally, the best way to model the incident muon flux on an experimental site is to perform a Monte Carlo simulation with a dedicated framework, for example CORSIKA ([Heck et al., 1998](#)). Unfortunately, this is a rather tedious work, as the trajectory of every single particle has to be simulated. For the Monte Carlo simulation to be statistically meaningful many particles have to be calculated, which takes a significant amount of time. This circumstance becomes worse if the Monte Carlo flux simulation has to be included in a Monte Carlo inversion (as will be explained in Ch. 2.5.3). This might even be prohibitive as the computational power is not good enough to produce results in a useful amount of time. We therefore prefer an analytical form of the muon flux model to improve the calculation’s performance, while still conserving the correctness of the model. A showcase of four frequently used muon flux models is made in Appendix A1.

2.2.2. Application to muon tomography

The starting point in muon tomography usually lies in deciding which differential muon flux (see Appendix A1) one wishes to use. The differential muon flux, $d\phi/dE$, denotes the number of muons that arrive at a certain height above sea level, from a certain direction (zenith &

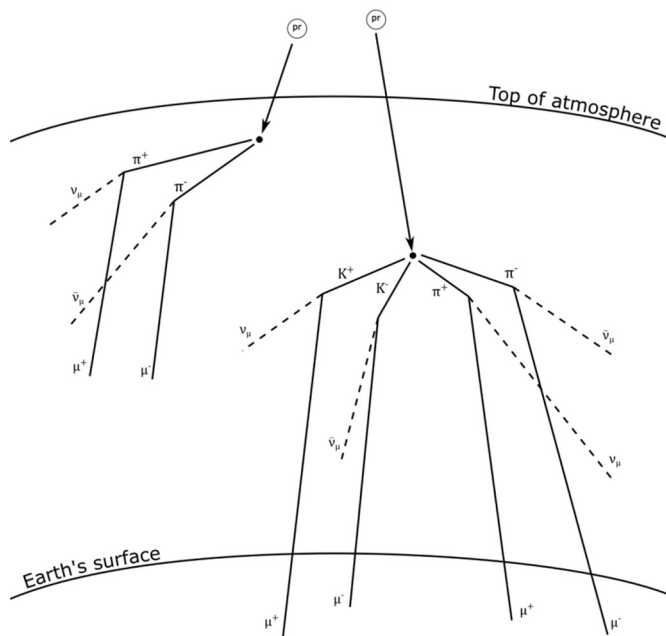


Fig. 3. Interactions of primary cosmic ray particles (pr) when they interact with atoms in the upper atmosphere (●). Simplified version of [Fig. 1](#) of [Gosse and Phillips \(2001, p. 1486\)](#).

azimuth angles) with a certain energy. Generally however, one does not use the differential muon fluxes directly, because this would require a measurement device that is capable of resolving the energy of the incident particle precisely. As a consequence, most present-day muon tomography experiments rely on the measurement of the integrated muon flux (e.g. Lesparre et al., 2010). Therefore, one only measures the presence of a muon and does not consider its energy. This becomes clear if one envisions the operation principles of the various detectors in the corresponding chapter (2.4). This limitation to an integrated flux may be expressed by an integral formulation for the differential fluxes presented above. Because one generally measures only muons above a certain energy threshold, the integrated flux can be written as

$$\Phi(E_{\text{cut}}) = \int_{E_{\text{cut}}}^{\infty} \frac{d\Phi}{dE} dE \quad (4)$$

where the integrand is any (differential) flux model one considers to use (see Appendix A1 for a selection thereof). In order to assess the uncertainty on the flux model, we employed a straightforward scheme. For the location of Bern, Switzerland (Lat: 46.94°N, Lon: 7.44°E) we calculated the differential and integrated variants of the four muon fluxes introduced above. Although the city of Bern is situated at around 550 m above sea level, we scaled the muon flux to sea level for the sake of comparability to other fluxes. To portray their differences in a clearer way we also calculated their ratio to the mean flux, which is given by a simple arithmetic mean,

$$\left\langle \frac{d\Phi}{dE} \right\rangle = \frac{1}{4} \left(\frac{d\Phi_T}{dE} + \frac{d\Phi_{RB}}{dE} + \frac{d\Phi_{RH}}{dE} + \frac{d\Phi_S}{dE} \right) \quad (5)$$

as well as the respective standard deviation,

$$\sigma_{d\Phi/dE} = \frac{1}{3} \sqrt{\sum_i \left(\frac{d\Phi_i}{dE} - \left\langle \frac{d\Phi}{dE} \right\rangle \right)^2} \quad (6)$$

where $i \in \{T, RB, RH, S\}$ denotes the four muon flux models in Appendix A1. Analogously, we computed the mean and the standard deviation of the integrated flux models $\langle \Phi \rangle$, σ_Φ . The resulting plot for vertical muons (i.e. $\theta = 0^\circ$) is shown in Fig. 4. Please refer to Appendix A2 for the respective plots of higher zenith angles ($\theta = 45^\circ$, 60°). The 1σ -uncertainty on this mean flux has been calculated by

$$\varepsilon_{\text{diff}, \pm 1\sigma} = \frac{\left\langle \frac{d\Phi}{dE} \right\rangle \pm \sigma_{d\Phi/dE}}{\left\langle \frac{d\Phi}{dE} \right\rangle} \quad (7)$$

and

$$\varepsilon_{\text{int}, \pm 1\sigma} = \frac{\langle \Phi \rangle \pm \sigma_\Phi}{\langle \Phi \rangle} \quad (8)$$

where the indices "diff" and "int" refer to the differential and integrated flux, respectively.

If the scope is to attach an uncertainty to a flux model, the purple line

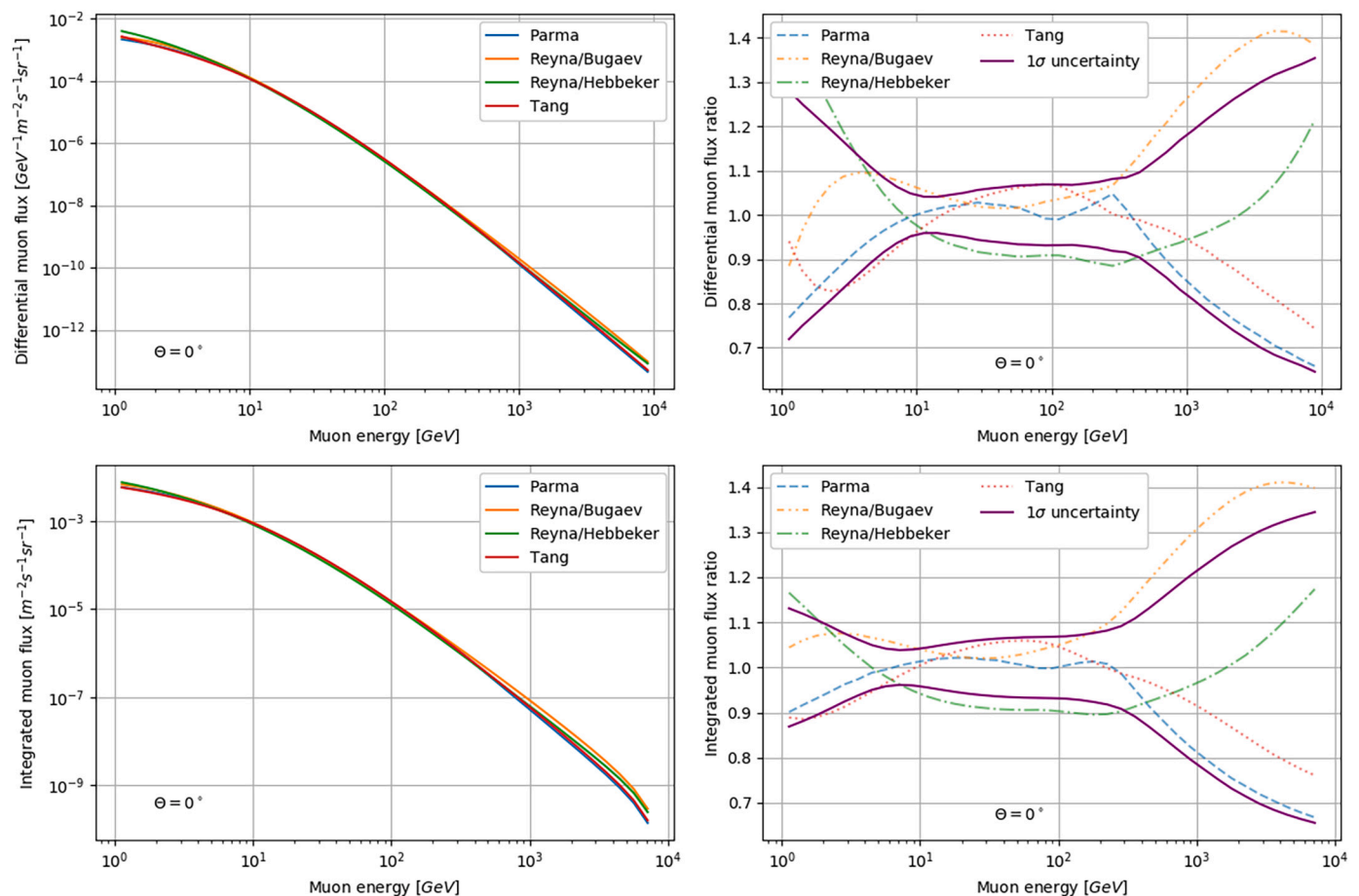


Fig. 4. Comparison of the four muon flux models (see Appendix A1.1 – A1.4) including an uncertainty estimate for a zenith angle of $\theta = 0^\circ$. *Top left:* Differential muon flux as a function of energy. *Top right:* Ratio between the differential muon flux and the mean differential flux $\langle d\Phi/dE \rangle$ (see Eq. (5)). *Bottom left:* Integrated muon flux as a function of the lower integration boundary (i.e. E_{cut} in Eq. (4)). *Bottom right:* Integrated muon flux ratio to the mean integrated flux $\langle \Phi \rangle$. The 1σ -uncertainty in the right-hand side plots has been calculated according to Eqs. (6) & (7).

in Fig. 4, Figs. A1 and A2 may be used. Muon tomography experiments for geological purposes usually operate in environments with material thicknesses of few 10 m to 1 km of rock, although 1 km is already considered as a thick mass of rock. This corresponds to an energy range of about 10 GeV to 1 TeV (The origin of these numbers is explained separately in Ch. 2.3). Instead of using the precise value of the error envelope, we may also attribute a conservative error estimate to the flux of around 15% (Hebbeker and Timmermans, 2002), which is a commonly used value in the community. This constant error simplifies the description of the uncertainties because it is now independent of the energy. There is also a specific reason for the conservative error estimate. We have computed the error based on four selected muon flux models only to get a rough overview. Accordingly, a conservative approach is reasonable in order not to exclude a higher variation due to other models.

The above presented muon flux models are equally suitable for the use in experiments. They can also be easily exchanged as the different models lie within the 15%-uncertainty boundary in the typical working energy range. We, however, found that the simple parametrisation by Reyna/Bugaev (see Appendix A1.2) is a good starting point for the application in an experimental campaign. Of course different muon flux models should be tested during the experiment and the most suitable one should be chosen and employed.

2.2.3. Factors affecting the muon flux model

Apart from the different muon flux models, there are additional geophysical factors, such as the Earth's magnetic field or the weather conditions that may affect the muon flux. This topic is discussed in Ch. 2.2 of Lesparre et al. (2010) in detail and we therefore limit ourselves to a short summary of that chapter.

The most important factor is the height of the measurement point. Any of the above-mentioned flux models may be scaled to another altitude by the relation (see for example Hebbeker and Timmermans, 2002)

$$\Phi_i(h) = \Phi_i(0) \cdot \exp\left(-\frac{h}{h_0}\right) \quad (9)$$

Here $h_0 = 4900 + 750 p$ is in metres and p denotes the muon's momentum. Users may find that another local scaling height, h_0 , may be more appropriate to describe the local muon flux. This has for example been done by Nishiyama et al. (2017), where $h_0 = 3400 + 1100 p$, according to the results of a Monte Carlo simulation.

A second important effect concerns the atmospheric density variations over the cycle of the year. As temperature changes during the different seasons, so does the density of the air, which may impact the muon flux model. This factor is important if one aims to reconstruct a time dependent signal, which might, for example, be related to changes in a magma chamber of a volcano. Lesparre et al. (2010) show how the related effects may be corrected for. Additionally, we refer the reader to Jourde et al. (2016), who experimentally investigated the effects of atmospheric changes (i.e. temperature and pressure) on muon flux measurements. It also provides the reader with information on how to deal with this effect when the thickness of the muon tomography target is rather low (i.e. some metres up to a few tens of metres of material).

2.3. Energy loss of muons in matter

In the preceding chapter we have presented how muons are produced in the outer atmosphere and how one can describe the amount of these particles showering down on Earth using a muon flux model. The next step in the journey of such a muon towards the detector, usually involves the penetration of a given thickness of material. By various interactions with the electrons and nuclei within the matter, the muon (which is also a charged particle) loses energy as it traverses the solid body. We note here that the matter does not have to be in a solid state

but may also be fluid or even gaseous. The processes of energy loss remain the same. However, in most practical muon tomography experiments the body in question is almost always a solid.

2.3.1. The energy loss equation

The processes of energy loss are well explained in Groom et al. (2001), and we gladly refer to this work and the references therein for detailed discussion of the involved theory of particle physics. The resulting energy loss equation takes the form of a first order ordinary differential equation,

$$-\frac{dE}{dx} = \rho(x) \cdot [a(x, E) + E \cdot b(x, E)] \quad (10)$$

where E is the energy of the muon, x its position along the path, $\rho(x)$ the density of the traversed matter and $a(x, E)$ & $b(x, E)$ the ionisation and radiative energy losses, respectively. By ionisation one refers to the excitation and/or ionisation of atomic electrons in the matter that were given some energy from the incident muon, whereas the radiation term encompasses the bremsstrahlung, the electron-positron pair production, and the photonuclear interactions. Important here is the fact that ρ , a & b are matter dependent properties. Groom et al. (2001) provide an energy loss list, where they tabulate dE/dx for each element and selected compounds. Unfortunately, the only geologically relevant materials are SiO_2 , CaCO_3 and an entity called "standard rock". An earlier work (Lechmann et al., 2018) addressed this problem and showed, in which cases this standard rock is a valid approximation and when it should be exchanged with a more realistic rock model that includes information on the composition. The Lechmann et al. (2018) study also provides energy loss calculations for several major rock types (i.e. granite, limestone, basalt) and developed a simple method to account for these different compositions. The result for a realistic rock model yields an energy loss formula in the same form as Eq. (10), i.e.

$$-\frac{dE}{dx} = \{\rho(x)\}_{\text{rock}} \cdot [\{a(x, E)\}_{\text{rock}} + E \cdot \{b(x, E)\}_{\text{rock}}] \quad (11)$$

such that all subsequent calculations can be treated equally. In summary, one should consider a realistic rock model if the rock is either basalt or limestone and features an expected thickness of more than 300 m. If these criterions are not met one is usually fine using the standard rock approximation.

2.3.2. Solution of the energy loss equation

There are multiple ways to solve Eq. (11), all of which share one common first step. We have to assume that the physical parameters are homogeneously distributed throughout our material block. In this case, it is possible to represent the material with a set of constant parameters. If this can be reasonably achieved, the most straightforward method would be to program a numerical solver for Eq. (11). Usually for this kind of problem a Runge-Kutta integration scheme (e.g. Stoer and Bulirsch, 2013) is sufficient. Naturally, any higher order numerical scheme is also possible. However, in any case they have to be compared to already existing calculations, as the numerical errors in these solvers have not yet been investigated systematically when applied to the energy loss equation. Alternatively, it is possible to recast Eq. (11) as an integral,

$$L(E) = \int_{E_0}^E dx = \int_{E_0}^E \frac{1}{\rho \cdot [a(E') + E' \cdot b(E')]} dE' \quad (12)$$

where E_0 "is sufficiently small that the result is insensitive to its exact value" (Groom et al., 2001). A good value can be chosen around several MeV. The range 10 MeV – 100 MeV is reasonable as muons in this energy range only penetrate a few centimetres into a material. Moreover, this range is also considered by the energy loss tables, which makes it easier to use if one does not want to implement a sophisticated solver. An example of such an energy loss table and information on where it may be

retrieved can be found in Appendix B. The parameter L in Eq. (12) denotes the penetration distance, which is usually presented in centimetres (depends on the units of a , b & ρ). Instead of L , however, the range R is often reported in physics literature. This quantity relates to the penetration distance as follows:

$$R(E) = L(E) * \rho = \int_{E_0}^E \rho(x) dx = \int_{E_0}^E \frac{1}{[a(E') + E'^*b(E')] dE'} \quad (13)$$

Eq. (13) has the advantage that the results are better comparable if the equation is applied to different materials. Please note that the second equality sign in Eq. (13) only holds for homogeneous media, where the material parameters do not change spatially. In applications with muon tomography, however, it is more convenient to use the penetration distance L of Eq. (12), even though these two equations convey the same information. In Table B1 of Appendix B one can also verify that the usual initial muon energies lie between 10 GeV and 1 TeV for penetration ranges L between 10 m and 1 km.

As Groom et al. (2001) provide energy loss and range tables for selected materials it is useful to keep in mind the relation between $R(E)$ and $L(E)$, see Eq. (13). It is thus also possible to adapt these tables for a version where the densities are modified. Thus, a “standard rock” with modified density may be used in scenarios, where the actual rock density is not exactly 2.65 g cm^{-3} . This inherently assumes no variation in composition, as only density changes are considered. Please refer to Lechmann et al. (2018) for more information about how this can be achieved in geological settings. In the aforementioned article, the reader may also find additional information on the exact geochemical and mineralogical composition of this standard rock. These authors also discuss how to proceed if a more realistic rock model is required and when this is required.

We conclude this section with a cautionary note. Even though Eqs. (12) & (13) may prove very useful, one has to consider that some part of the ionisation losses, $a(E)$, is dependent on the density, such that the

right-hand side of the equation would change with different densities. If the modified densities are close (within $\sim 5\%$) to the tabulated density (again for standard rock this is 2.65 g cm^{-3}) one should, however, be fine upon employing Eqs. (12) & (13). At this stage, we know of no publication where this possible bias has been systematically analysed within a geological context.

2.3.3. Multiple scattering

The calculations listed above represent already a good model, which should suit the needs for many applications. However, they carry an implicit assumption one has to be aware of. In particular, the solution to the energy loss equation assumes that muons penetrate the matter of interest along a straight path, i.e. a line. This does, however, not reflect reality. In fact, the muon is continuously deflected by small angles upon travelling through the material. These angles sum up, and upon leaving the material the muon may find itself within a cone, where the centre axis represents the perfectly straight path that is usually considered. Tanabashi et al. (2018) provide the following scheme (see Fig. 5a) to illustrate the problem.

In this context, we are mainly interested in the quantity θ_{plane} . This is a measure of the angular deviation of a muon after crossing a definite thickness of rock. The consideration of such a deviation is important if the angular resolution of the detector is used as a reference. This then leaves the question of how to calculate θ_{plane} . For this purpose, we may use Highland’s formula (see e.g. Lynch and Dahl, 1991)

$$\theta_{\text{plane}} = \frac{13.6}{\beta pc} \sqrt{\frac{\lambda}{\Lambda_0}} \left[1 + 0.088 \log_{10} \left(\frac{\lambda}{\Lambda_0} \right) \right] \quad (14)$$

where, p is the momentum of the muon, c is the speed of light, $\beta = v/c$ a relativistic parameter and λ is the thickness of the material in density length units (i.e. $[\text{g cm}^{-2}]$). This can be obtained by $\lambda = \rho_{\text{rock}} * x$, where x is the thickness in $[\text{cm}]$. Finally, Λ_0 is the radiation length of the

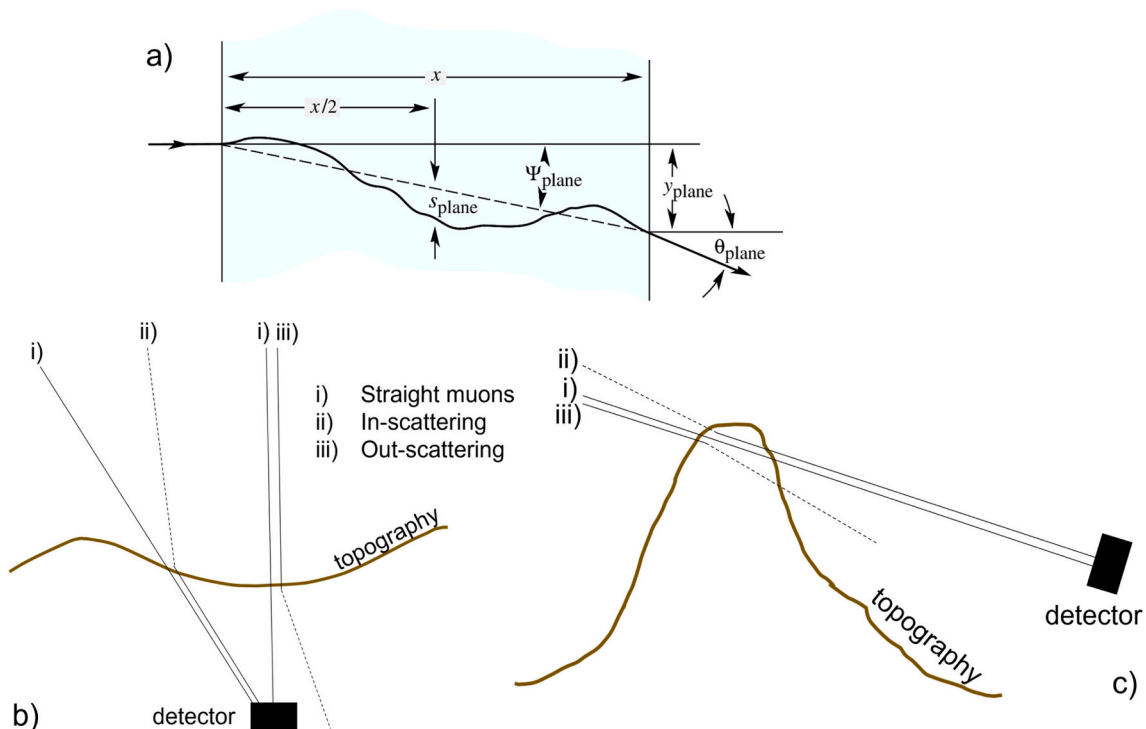


Fig. 5. a) Scheme to illustrate multiple coulomb scattering of an incident particle (Fig. 33.10 of Tanabashi et al., 2018, p. 452.) A particle hits a block of matter with thickness x and is continuously deflected. It exits this block with a mean angular deflection of θ_{plane} and an offset of y_{plane} . For the other quantities, which we do not need for further computations (i.e. Ψ_{plane} , s_{plane}) we refer the reader to the original source of this diagram. b) & c) show how multiple coulomb scattering affects the muon flux measurements underground (b) or above ground (c) through in- and out-scattering of muons. Here straight lines denote paths, that hit the detector whereas dashed lines indicate muon travel paths that do not hit the detector.

material that can be obtained by the formula of Tsai (1974),

$$\frac{1}{\Lambda_0} = \frac{Z^2 [L_{\text{rad}} - f(Z)] + ZL_{\text{rad}}'}{716.405 A} \quad (15)$$

The term $f(Z)$ in Eq. (15) may be calculated by

$$f(Z) = (\alpha Z)^2 \left[(1 + (\alpha Z)^2)^{-1} + 0.20206 - 0.0369(\alpha Z)^2 + 0.0083(\alpha Z)^4 - 0.002(\alpha Z)^6 \right] \quad (16)$$

where Z is the atomic number of the element and $\alpha = 1/137$ is Sommerfeld's constant. The two auxiliary quantities L_{rad} , L_{rad}' have to be chosen according to Table 1.

Unfortunately, it is often the case that we need to know Λ_0 not for a pure element but for a rock, which is a mixture of elements. To solve this problem, we could conduct the aforementioned calculations for a standard rock, for example. Lesparre et al. (2010) as well as the PDG (Particle Data Group; <https://pdg.lbl.gov>) list the radiation length for standard rock as $\Lambda_{0, \text{SR}} = 26.54 \text{ g cm}^{-2}$.

But generally, we want to calculate the radiation length of a mixture of elements (Tanabashi et al., 2018) by

$$\left\langle \frac{1}{\Lambda_0} \right\rangle = \sum_j w_j \frac{1}{\Lambda_{0j}} \quad (17)$$

Here, w_j is the weight fraction of the j -th element in the compound and $\Lambda_{0, j}$ is the radiation length of the j -th element, respectively. We show in Appendix C how the user may derive a radiation length, given some XRF (X-ray fluorescence) measurements. The resulting radiation length for our exemplary “real” rock is $\Lambda_{0, \text{rock}} = 25.72 \text{ g cm}^{-2}$.

Please note that even though the difference is $\sim 3\%$ and thus very small considering the overall scheme, our host rock that we measured in Nishiyama et al. (2017) had a rather granitic composition. As shown in Lechmann et al. (2018) granitic rocks tend to be well approximated by the standard rock, while others may not. We recommend performing an analogous calculation as shown in Appendix C for every experiment, even if one has no XRF data at hand and has to rely on a rough (usually macroscopic) description of the lithology.

With this $\Lambda_{0, \text{rock}}$ it is now possible to calculate the scattering parameters from Fig. 5a. Unfortunately, Eq. (14) is only valid for a relatively thin absorber, where the energy stays roughly constant, i.e. the energy loss is negligible. As Lesparre et al. (2010) state, we need a differential form of Eq. (14) to also account for the energy, which is lost during the passage through matter. Even though they do not provide the differential form, one might get an idea from the CERN report of Schwarz (2013), where the total deviation is calculated by adding the “thin slab”-contributions together in quadrature, taking into account the energy loss. Tailoring this idea to Eq. (14) yields

$$\theta_{\text{plane}} = 13.6 \left[1 + 0.088 \log_{10} \left(\frac{\lambda}{\Lambda_0} \right) \right] \left(\frac{\rho_{\text{rock}}}{\Lambda_{0, \text{rock}}} \int_0^D \left(\frac{1}{\beta pc} \right)^2 dx' \right)^{1/2} \quad (18)$$

Note that this is already the integrated formula for a thick absorber such as a mass of rock. One would end up with a similar result when the original formula from Lesparre et al. (2010) would be used. The only difference lies in the integrand (i.e. $(\beta pc)^{-1}$ vs. E^{-1}). This may be explained by the high energy nature of the experiments in the field of

Table 1

Table 33.2 of Tanabashi et al. (2018, p. 452). Key on how to calculate the quantities L_{rad} and L_{rad}' necessary for Eq. (15).

Element	Z	L_{rad}	L_{rad}'
H	1	5.31	6.144
He	2	4.79	5.621
Li	3	4.74	5.805
Be	4	4.71	5.924
Others	>4	$\ln(184.15 Z^{-1/3})$	$\ln(1194 Z^{-2/3})$

muon tomography. Usually, these kinds of studies require muon energies on the GeV level. βpc may be expressed as $(\gamma - \gamma^{-1})m_\mu c^2$. When energies are high, then $\beta \rightarrow 1$ and $(\gamma - \gamma^{-1}) \rightarrow \gamma$, such that $\beta pc \rightarrow \gamma m_\mu c^2 = E$. For example, a 1.05 GeV muon has $\gamma \approx 10$ and thus the difference between the two different formulae is 1%. As 1 GeV is rather a lower threshold, one should be fine in using the energy approximation

$$\theta_{\text{plane}} = 13.6 \left[1 + 0.088 \log_{10} \left(\frac{D \rho_{\text{rock}}}{\Lambda_0} \right) \right] \left(\frac{\rho_{\text{rock}}}{\Lambda_{0, \text{rock}}} \int_0^D \left(\frac{1}{E} \right)^2 dx' \right)^{1/2} \quad (19)$$

Table 2 shows the calculations of θ_{plane} for standard rock for different thicknesses, D , and exit energies, E_{ex} , (i.e. energy of the muon after the thick absorber).

We note that θ_{plane} is only weakly dependent on the thickness of the absorber and more sensitive to the exit energy of the muon. This has a rather direct implication on how the detector needs to be constructed (we briefly address this issue in Ch. 2.4).

First, these θ_{plane} values are a lower threshold for the angular resolution that we may achieve, irrespective of the actual angular resolution of the detector. Second, according to Fig. 5b one would expect that certain muons are deflected away from the detector (out-scattering) and thus reducing the measured muon flux from the observed direction. Additionally, there would also be a part of the muon flux that would initially not hit the detector if the muons were to propagate on a perfectly straight trajectory but is deflected into the detector. This so-called in-scattering would then increase the muon flux from the apparent incidence direction of the muon (assuming a straight path). For the case of an underground measurement (see Fig. 5b) we argue in Appendix D that in- and out-scattering usually cancel each other out and do affect our measurements only through a “blurring” effect. These two biases (but especially the first one) can be rather well mitigated by building the detector in a way that allows only to register those muons with a sufficiently high energy. Thus, one gains some control over this rather difficult problem. The possible bias that results from the sensitivity of the equations is also discussed in Lesparre et al. (2010) and attributed to the fact that in Eq. (19) we integrate over $1/E^2$. This means that the muons are scattered more the slower they become, i.e. during the very last part of their trajectories.

In the case of a muon flux measurement above ground (see Fig. 5c) the situation is different. Here the problem may arise that a portion of the open-sky muon flux enters the mountain in the very top layers (a few metres) and is deflected towards the detector. With the same reasoning as above (see Appendix D) also a part of the originally straight muons is deflected away from the detector. However, due to the power-law nature of the muon flux (see Fig. 4) the part of the in-scattered open-sky muon flux is much larger than the out-scattered portion (as these muons have already penetrated much more material, they consist of the part of the muon flux that had initially a higher energy). Accordingly, around the edges of the mountain a too high muon flux may be measured that should be corrected for.

At this point we would like to raise one final issue concerning the muon flux measurements above ground. As mentioned in Jourde et al. (2013) the existence of an upward-going muon flux is not described by any muon flux model from Appendix A1. The origins of this flux are still under investigation. However, as a practitioner one needs to be aware of

Table 2

Calculations of the mean angular deviation, θ_{plane} , for different absorber thicknesses, D , and different muon exit energies, E_{ex} .

D [m]	50	150	300
E_{ex} [GeV]	θ_{plane} [mrad]		
0.1	316.53	316.71	316.74
1	77.34	78.04	78.18
10	19.85	21.57	22.00
100	3.39	4.69	5.30

this effect, especially when the detector is stationed above ground. In that case measured muons from this upwards-directed muon flux may be erroneously taken for muons from the actual cosmic ray flux described with the models in Appendix A1, which can lead to a serious bias in the measurement. Jourde et al. (2013) discuss where this problem may appear and present several ways how to deal with it. If the detector is, however, located underground, then the surrounding material is usually enough to shield the measurement device from the upward-going muons.

2.4. Detectors

In this chapter we present the detectors that are commonly used in a muon tomography experiment, so that the user may form an own idea, which device may be suitable for his/her own research. As our own expertise lies with the application of nuclear emulsion films (Nishiyama et al., 2017), we will portray the corresponding detector type in more detail. However, we will also present the other technologies, summarise them and redirect the user to studies for more information and/or applications. In general, muon detectors are passive detectors as they only record the naturally occurring cosmic ray muon flux at a position in a certain direction. The main difference of the following detector types lies in their deployment conditions that are closer described in the respective sections.

2.4.1. Nuclear emulsions

The concept of how nuclear emulsions work may probably be best described through a comparison to photographic films that were used decades ago. We also have used such a detector in our own experiments (Nishiyama et al., 2017; Nishiyama et al., 2019). An overview of how we built our detectors and processed the data can be found in Ariga et al. (2018) and we limit our presentation here to the most important production and data processing steps.

Fig. 6 shows a sketch of how an emulsion film is built up and how it works. Even though the setup for one emulsion film looks rather straightforward, their production may be complicated. A short overview over the different production steps can be found in Morishima et al. (2017). The result is a doubly layered emulsion film that is vacuum-packed in a completely lightproof sleeve (see Fig. 5. of Morishima et al., 2017). For visibility reasons, the sleeve has been omitted in our Fig. 6.

The right panel of Fig. 6 shows the principles of how emulsion films register incoming and outgoing muons. In particular, when muons hit the prepared muon film, then parts of the silver-bromide crystal are broken up into bromide and silver ions. The latter tend to aggregate on the surface of the crystal and form a latent image, which then show up as clusters (i.e. stars in Fig. 6) when the film is developed in the laboratory. In each emulsion layer a linear sequence of clusters can be assembled to a “microtrack” (see solid black lines in Fig. 6). Through the matching of microtracks from the top and the bottom layer on one film one may

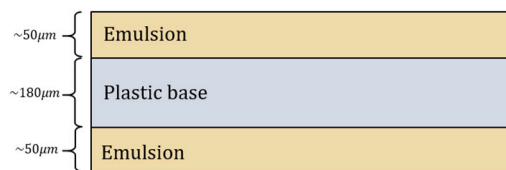


Fig. 6. *Left:* Structure of a single emulsion film. It consists of a plastic base ($\sim 180\ \mu\text{m}$) coated on both sides with a photosensitive (i.e. contains AgBr-crystals) emulsion ($\sim 50\ \mu\text{m}$). *Right:* Schematic view of the state of an emulsion film when it is developed after exposure to the cosmic ray muon flux. Stars indicate activated AgBr-crystals (i.e. clusters; they will show as dark grains). Black lines connecting clusters are reconstructed particle tracks. Muons are assumed to propagate straight through the detector. Dashed red lines denote the part of the muon track within the emulsion, whereas the solid red lines indicate the “basetrack”, i.e. the unobserved muon track within the plastic base. (For interpretation of the references to colour in this figure legend, the reader is referred to the web version of this article.)

construct so called “basetracks” (i.e. tracks of muons that must have penetrated the whole film, including the plastic base; see solid red lines in Fig. 6). However, as this film also records tracks in the time span between the production and the deployment at the experimental site, one would have to deal with a hard signal-noise separation problem. One possible solution to this problem is to build the emulsion detector in a ECC (emulsion cloud chamber) arrangement (Nishiyama et al., 2014, 2015).

The principle is to form a “sandwich” of single emulsion films interlaced with metal plates as depicted in Fig. 7. This arrangement of the detector has two big advantages. First, the ECC structure may be assembled upon arrival at the experimental site, and one is sure to only record muon tracks from the study site. The trick lies in the fact that one only has to consider muon tracks that penetrate the whole detector. These tracks and their orientations may be reconstructed using the same logic (i.e. alignment of the different layers) as the processing step from microtracks to basetracks. Second, the addition of metal plates acts as an artificial threshold to filter out the low energy particles. This filtering occurs mainly through the deflection of low energy particles at a higher angle, such that they do not appear as straight tracks anymore. This means that also electrons that may produce a substantial bias, or even worse a background noise within the films, are filtered out and do not significantly contaminate the measurement (Nishiyama et al., 2015). Therefore, such a detector setup is better suited for geological purposes than an emulsion film detector that is made up of one single layer only, because it considerably facilitates the data processing afterwards. For an example image we refer to Fig. 8, where two of our deployed instruments in Nishiyama et al. (2017, 2019) are shown.

Emulsion detectors are thus very versatile and, once packed in a lightproof sleeve, relatively easy to handle and transport. The most outstanding feature, however, is the fact that emulsion detectors do not need any form of electric power supply. They collect the data passively and continuously, which means that there is theoretically no dead time in the detector. This enables scientists to place these detectors in tunnels

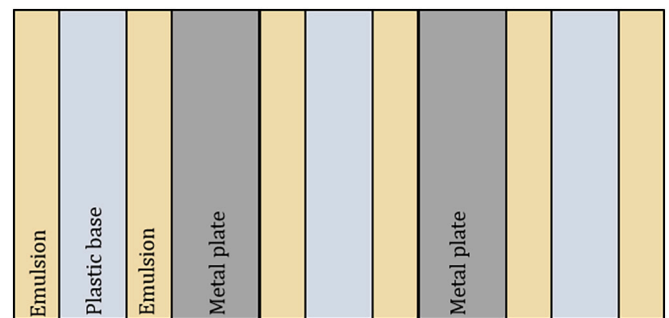


Fig. 7. Arrangement of emulsion cloud chambers (ECC). This type of emulsion detector consists of alternating layers of emulsion film and metal plates.

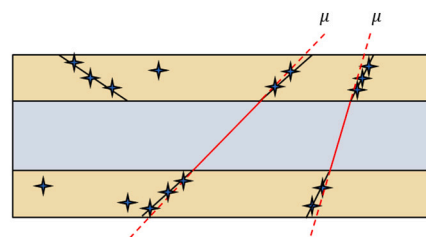




Fig. 8. ECC detector frames that were deployed in our previous projects (Nishiyama et al., 2017, 2019). We used two different setups with different sizes. *Left:* Small scale detector consisting of two ECC pouches with a total detection area of $\sim 250 \text{ cm}^2$. *Right:* Large scale detector consisting of four ECC pouches with a total detection area of $\sim 1.2 \text{ m}^2$. Humans are included for scale.

underground or other remote places in the mountains, without having to worry about excessive hauling or, as said, installing an equipment for power supply.

These advantages do not come without any significant drawbacks. In comparison to the other detectors, we sacrifice the ability to retrieve time resolved data. In particular, emulsion detectors record a time-integrated signal, and one has no chance of reconstructing, which track has been recorded at what time and under what conditions. Additionally, emulsions require a rather long pre- and post-processing time. This means that the production of emulsion films, their development in the dark chamber as well as their scanning may take some time. Finally, emulsion detectors can lose their recorded signal (“fading”) if the film is exposed for too long a time span ($> 3\text{--}4$ months). In addition, the equipment has to be kept always around the same temperature and humidity conditions, because any fluctuations of these parameters may favour the occurrence of premature fading.

2.4.2. Scintillators

A second type of detector that has been widely employed in muon tomography studies are scintillators. Here the incoming charged particles excite the electrons of the scintillating material to higher energy levels. These electrons fall back into their ground state, thereby releasing energy in form of a photon. The latter is then often detected by a photomultiplier and converted into an electronic signal (see also Lesparre et al., 2010; Gibert et al., 2010; and Pla-Dalmau et al., 2001, for more information). The scintillation detectors are in a way the opposites of the emulsion detectors. The former need an external power supply, which is often provided by a photovoltaic panel (e.g. Gibert et al., 2010). Thus, much of the detector design is focused on the power consumption to render the detector energetically self-sufficient. By recording each particle live, it is possible to record the muon flux in real time, even if the flux will then be manually time integrated during the subsequent processing steps. Therefore, on the positive side, one may keep the control over the integration step, such that possible seasonal effects may be analysed. On the downside, scintillation detectors may consist of too many heavy parts, which make the transport and the installation difficult to organise. Furthermore, by using scintillation bars one often has to limit the angular resolution of the detector, as these bars cannot be made arbitrarily small. Another point to consider is the dead time of the detector (as with nearly every real time detector). Once the detector records a track, it needs to recharge and cannot record another track during this time. Ambrosino et al. (2015) report the dead time in the order of 20% for their scintillation detector. For readers interested in how such a detector looks like, please see Fig. 9.

2.4.3. Gaseous detectors

A further type of detector uses a gas to record a charged particle's

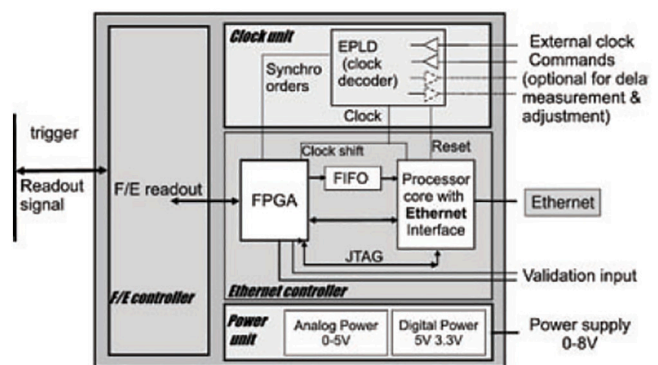
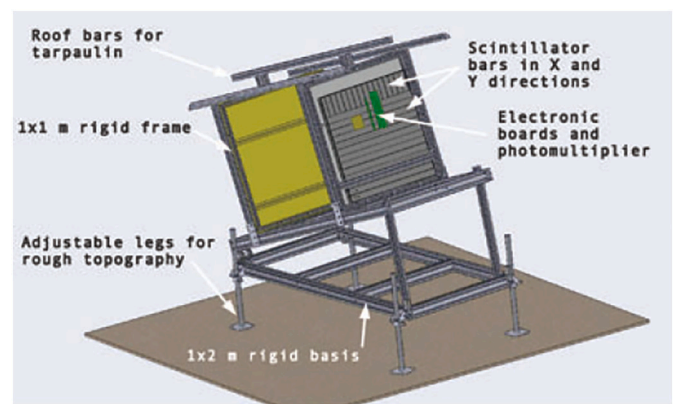


Fig. 9. Fig. 5 from Lesparre et al. (2010). *Top:* Sketch of a muon detector consisting of horizontal and vertical scintillator bars. *Middle:* Electronics of the muon telescope. *Bottom:* Example of two muon detectors deployed in the field.

presence and movement (see Fig. 10). When a charged particle traverses the gas, then its electrons are ionised. As the gas is enclosed by an anode and a cathode, both of which maintain an electric field, the ionised

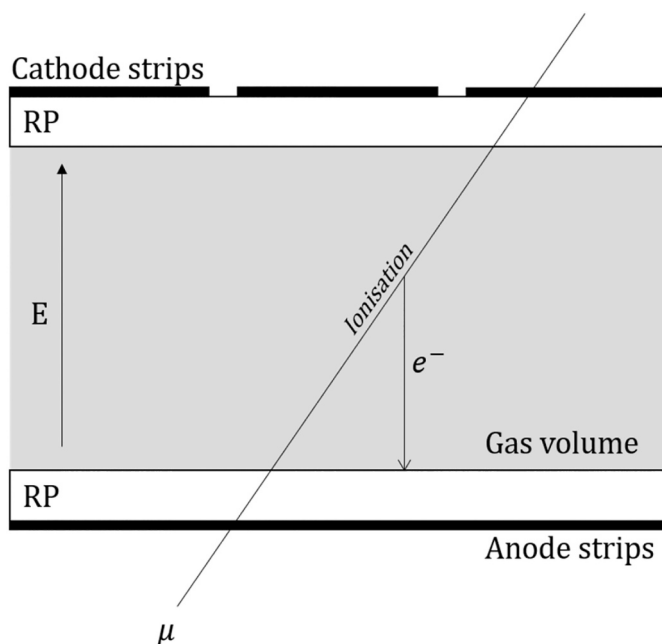


Fig. 10. Principle of a gaseous detector. A charged particle (here a muon) crosses the gas and ionises electrons along its trajectory. Due to the presence of an electrical field (E ; produced by the cathode/anode strips) the electron is accelerated towards the anode, producing an avalanche of even more electrons. The avalanche is usually large enough to induce a signal in the electrodes that may be read out. The resistive plates (RP) damp the electron avalanche in order to reset the detector (such that it can record a new particle). A segmentation of the cathode/anode into strips enables localisation of the particle.

electrons are accelerated towards the anode. This acceleration of the electrons initiates a chain reaction where further electrons are ionised thereby resulting in an electron avalanche. This, in turn, induces a signal in the electrodes that can then be measured. The interested reader is referred to [de Asmundis et al. \(2007\)](#) for further information on the resistive plate chamber (RPC) detectors. Another similar detector type that has been deployed for muon tomographic experiments is the Mircomegas detector (see e.g. [Giomataris et al., 1996](#)). This is basically a variant of the RPC detector.

[Fig. 10](#) shows the concept of one single detector layer, which, however, is not suitable to detect the directionality of the incident particle. For this reason, RPCs are usually deployed as stacks of multiple RPCs on top of each other, an arrangement which is often called a “hodoscope”. Accordingly, most particle detectors presented here fulfil the description of a hodoscope.

As a detector that records passing particles in real time, it features similar advantages and drawbacks as the scintillation detectors. The most important advantage is the time resolution of the recorded muon flux. The dead time in modern-day gaseous detectors is reported to be around 6% ([Ambrosino et al., 2015](#)) and can be even lower than 1% ([Varga et al., 2020](#)). On the negative side, the generation of an electrical field needs an external power supply, which may require more planning before an experiment.

2.4.4. Cherenkov detectors

The last instrument that we describe in this review is a rather niche detector. This type records the Cherenkov radiation that is emitted when a charged particle traverses a block of matter while exceeding the speed of light within the traversed matter. This may be best described by an analogy to the supersonic wave that is created when an object travels faster through the matter than its speed of sound, with the difference that the wave that is created in the Cherenkov process is an electromagnetic wave, i.e. a photon. We refer here to the study of [Catalano](#)

[et al. \(2016\)](#) who deployed a Cherenkov detector to perform a muon radiography experiment at Mt. Etna in Sicily, Italy. These authors also describe how the detector works, and they provide illustrative photographs that nicely show the dimensions of this device. As a real time detector, it has very much the same advantages as the other real time detectors as well as the need for an external power source. Moreover, due to its sheer size, this detector is probably more suited for a long-term, quasi-stationary observation ward (the mirror of the Cherenkov telescope in [Catalano et al., 2016](#), has a diameter of roughly 4 m).

There are also more recent developments that aim at reducing the size of the detector by hybridising with another detector type. For example [Vesga-Ramírez et al. \(2021\)](#) employed with their MuTe a hybrid telescope that uses two scintillator panels and a water Cherenkov detector.

2.5. Inversion schemes and tools

In this chapter we present several inversion techniques that are commonly utilised to invert results from muon tomography experiments. The selection of the corresponding approach mostly depends on the goal of the muon flux measurement, and the data analysis procedure is then often adapted accordingly. We also want to present a few tools that may be useful when designing and implementing an own inversion procedure. In all of the following approaches the trajectories are considered straight.

2.5.1. The density-length approach

This is by far the most used technique in muon tomography, mainly due to its simplicity. The idea comes from [Eq. \(13\)](#), where

$$\int \rho(x) dx = \Lambda \quad (20)$$

and Λ , the “density-length”, opacity, or range, can be calculated from the muon flux model and a material table (see [Ch. 2.3](#)) given some measurement results. Please note that the density-length, Λ , is not to be confused with the radiation length, Λ_0 , from [Eq. \(14\)](#). From the expression in [Eq. \(20\)](#) one can derive a wide array of parametrisations, i.e.

$$L_1 \cdot \rho_1 = \Lambda, \quad (21)$$

when only one material is present or

$$L_1 \cdot \rho_1 + L_2 \cdot \rho_2 = \Lambda, \quad (22)$$

for a stack of two different materials, etc. In any case [Eqs. \(21\) & \(22\)](#) are underdetermined and thus need additional information to resolve the involved parameters well. In case of [Eq. \(21\)](#) one usually knows the material thickness, L_1 , and tries to draw inferences on the mean density, ρ_1 . In many applications in the field of volcanology, this has been the preferred procedure, as one is mostly interested in mapping the density anomalies. [Eq. \(22\)](#) is an example, which could be used for an interface detection, i.e. one is interested in L_1 and L_2 . This can be solved by assuming that we know the densities ρ_1 & ρ_2 and the total material thickness $L_1 + L_2 = L_{\text{tot}}$. From this short discussion one sees that the growing number of parameters is countered with additional information, which is the only practicable way when facing an underdetermined problem. The popularity of this approach comes largely from its ease to use and the relatively robust result it produces.

The aforementioned approach is often formulated as a deterministic inverse problem, i.e. a least squares problem, that can be solved using a matrix equation. We refer here to [Nishiyama et al. \(2014\)](#) or [Barnoud et al. \(2019\)](#) for an example on how this may be set up. In those studies, the authors have combined muon tomography measurements with gravimetric measurements (a reasonable choice, as will be discussed in [Ch. 4](#)).

2.5.2. Bayesian approaches

As an alternative to solving the inversion deterministically (i.e. matrix equations), one may also employ Bayesian techniques that try to set up the problem in a probabilistic framework. Even though Bayesian approaches provide a large arsenal of techniques to tackle the inverse problem, their use in muon tomography is far from ubiquitous. The reason for this circumstance lies most probably in the intricacies of the design and the solution of a probabilistic model. Despite these problems, Bayesian methods have the advantage when information on parameters from various sources such as the results of laboratory measurements, literature data or even boundaries of parameter values, for example, have to be incorporated. As the probabilistic formulation remains the same these different datasets can be integrated with ease. In this approach, the physical laws take the form of surfaces within the multi-dimensional data-model space, in which each datum and each parameter has its own dimension. A comprehensive explanation of such an approach can be found in the book of Tarantola (2005). Barnoud et al. (2019) as well as Lelièvre et al. (2019) provide examples where a Bayesian approach has been used to merge gravimetric and muon tomography data within an inversion scheme. Other muon tomographic stand-alone studies were undertaken by Lesparre et al. (2012, 2017) and Vesga-Ramírez et al. (2021) by using a technique called simulated annealing. We refer the reader to Kirkpatrick et al. (1983) for the original paper on this technique or to Sivia and Skilling (2012), p.63, 203–208 for an introduction to the topic.

Even though we advocate in favour of using Bayesian methods, we have to stress that usually this comes at the price of having to solve the inverse problem by means of a Monte Carlo simulation, in order to properly sample the posterior probability density function. This is often associated with higher computational costs, and therefore the chosen algorithms have to be programmed carefully. For example, this does usually not allow for another Monte Carlo simulation (i.e. a muon flux simulation) to be performed within the Monte Carlo inversion. We think, however, that if care is taken in the design of the inversion, this should not pose a serious hindrance.

2.5.3. Alternative approaches & tools

As the approaches discussed in chapters 2.5.1 and 2.5.2 tackle the problem from a physical/geophysical point of view, efforts are also being made to exploit the similarity to medical applications like X-ray computed tomography (CT) or positron emission tomography. Nagahara and Miyamoto (2018) for example have studied the use of a technique called “filtered back projection”, which is widely used in X-ray tomography. Naturally, also other medical inversion methods, including the ones already used in the CT-industry, could potentially be adapted for muon tomography.

As the state of this technology is, however, still very much in its beginnings, no commercial software and therefore no standardised way exists for the processing of the data. Thus, for this last step in the whole data processing chain, one is often confronted with the situation, that an own code has to be written. Here present a few tools that we think are useful if one desires to develop an own application.

The first tool we refer to is GEANT4 (Agostinelli et al., 2003), an all-purpose toolkit to simulate particle transport through a variety of materials. In addition, with PUMAS, Niess et al. (2018) released a backward simulation modification, such that the Monte Carlo Simulation of the particles is sped up considerably, by only considering muons that actually hit the detector. In light of its use in gravimetric inversion, pyGIMLi (Rücker et al., 2017) might also prove useful if one wants to combine the measurement results from gravity and muon tomography surveys within a single inversion scheme. Moreover, in another study a toolkit, SMAUG (Lechmann, 2021), is provided that allows the user to perform a Bayesian inversion of muon flux data with customisable materials.

3. Recent applications

In this chapter we present an overview of the recent applications to redirect the reader to studies that might be useful for one's own research. This is intended to provide the reader with an idea on how muon tomography can be applied in the specific contexts. We focus solely on geological examples, as other reviews that are listed in previous chapters cover the other fields (mostly archaeology and civil engineering) in great detail.

In general, muon tomography can be applied in two main ways. First, this technology allows to detect regions of relatively high/low density. Such features are often encountered in volcanological research (e.g. Tanaka et al., 2005; Oláh et al., 2019) where the aim is to visualize the corona region of a volcano. The other possibility is to detect boundaries with a high-density contrast. This has for example been performed in a glacial environment where the scope was to detect the base of a glacier, (e.g. Nishiyama et al., 2017) or in a tunnel where the aim was to investigate the location of a (low-density) karstic network (see Lesparre et al., 2017). Most of the muon tomography studies fall into either of the two categories. We have compiled a list of recent application of muon tomography to tackle geoscientific questions in Table 3.

4. Best practice guidelines

We would like to conclude our review with a guide on how a (geo) scientist who is interested in utilising this technology might proceed. In the subsequent paragraphs we define various criteria, which, we think, a prospective user must ask him-/herself whilst preparing a project. Even though the points we raise are also valid for many other geophysical methods, here, they are set in the context of muon tomography experiments. We split the basic planning steps in two parts. Whereas Ch. 4.1 explains the basic planning steps before deciding on whether to use muon tomography or not, Ch. 4.2 focuses more on some technical questions regarding the selection of the appropriate detector, the estimation of the timespan of exposure, and the search for alternative methods.

4.1. Planning phase

In this chapter we summarise four basic questions that should ideally be answered with “Yes” for muon tomography to be considered as a tool to be employed. These considerations can already be made in an early planning phase, where it is not already clear how the parameters of interest are supposed to be measured.

1) **Applicability:** “Is the method sensitive to the parameter in question?”

The first question a potential user must answer concerns the general applicability of the method to the problem at hand. Muon tomography is mainly sensitive to material density and density contrasts and only slightly to material composition. However, state-of-the-art muon tomography is not capable of resolving compositions very well, due to the systematic errors in the cosmic ray flux models. Thus, if the research question requires information about a 3D density structure, then muon tomography is a valid option.

2) **Alternatives:** “Is there another method that would yield more useful results?”

Intricately linked to the previous point is the question whether muon tomography is the optimal method for the problem at hand. We advise the prospective user to inform her-/himself if there are other geophysical methods that may provide better results. In this case one could ask if muon tomography is then a valid auxiliary method (considering that nowadays many experimental field campaigns do rely on multiple geophysical measurements).

Table 3
Selected publications of muon tomography experiments in geoscientific contexts.

Authors	Muon detector	Location	Summary
<i>Volcanology</i>			
Tanaka et al. (2005)	Plastic scintillator	Mt. West-Iwate, Honshu Japan	Muon tomographic and gravimetric data were collected on two Volcanoes (Mt. Kurokura & Mt. Ubakura). Alongside a density estimation of the volcanic lithology, a time dependent change in muon intensity was linked to volcanic activity. The observation lasted 1 year; the detector was designed to withstand also snowy weather conditions.
Tanaka et al. (2007)	ECC	Mt. Asama, Honshu, Japan	A survey, in which muon tomography was used to depict lithological density differences in the top region of the volcano. Density anomalies were related to volcanological structures of previous eruptions (lava cap, magma conduits). The device recorded for 2 months.
Tanaka et al. (2009)	Plastic scintillator	Satsuma-Iojima, Osumi islands, Japan	Imaging of the magma head in the main conduit of the Mt. Io volcano was performed. Degassing processes were identified and characterised according to the muon measurements.
Lesparre et al. (2012)	Scintillator	La Soufrière, Guadeloupe, France	This work presents relative 2D density distributions, retrieved from muon measurements. These were compared to separate electric resistivity and gravimetric models. Volcanic features were identified with the different observed structures in the various density models. Data acquisition took around 82 days.
Nishiyama et al. (2014)	ECC	Mt. Usu region, Hokkaido, Japan	This study combined measurements of gravimetry and muon flux of the Showa-Shinzan lava dome (side peak of Mt. Usu). A joint inversion, i.e. a 3D structural density analysis of the volcanic complex was performed, i.e. horizontal cross-sections for various altitudes across the volcano. The muon data

Table 3 (continued)

Authors	Muon detector	Location	Summary
Tanaka et al. (2014)	Plastic scintillator	Satsuma-Iojima, Osumi islands, Japan	was collected for 3 months. The muon flux measurements were used to depict a temporally resolved image of an eruption of the upper region of Mt. Io in 2013. The measurements were aggregated to periods of 3 days over the course of a month.
Ambrosino et al. (2015)	Plastic scintillator (MURRAY) Glass RPC (TOMUVOL)	Puy de Dôme, Auvergne, France	This work is a comparison of two different detector types from two independent measurement campaigns. This was done to unravel systematic errors that would be invisible from only one measurement.
Rosas-Carbajal et al. (2017)	Scintillator	La Soufrière, Guadeloupe, France	Joint 3D inversion of gravity and muon flux data that was compared to a conductivity model, received from electric resistivity tomography. The scope was to identify the volcanic hydrothermal system and its connection to the mechanical instabilities of the volcano's southern slope.
Oláh et al. (2019)	Multiwire proportional chamber (see Varga et al., 2016)	Sakurajima, Kyushu, Japan	This survey was done to investigate the possible formation of a magma plug in the volcano's conduit and its relation to the eruption frequency of two neighbouring craters. 2D tomographic images were produced to strengthen the empirical basis.
Tioukov et al. (2019)	ECC	Stromboli, Aeolian islands, Italy	A study where the scope was to determine the internal structure of the crater region and the north-eastern flank of the volcano with 2D tomographic images. Links between eruption dynamics and volcano structure were investigated. The detector was operated for 5 months.
Lo Presti et al. (2020)	Plastic scintillator	Etna, Sicily, Italy	2D tomographic images of the volcano's crater region were produced and used to monitor ongoing eruptions. Measurements were taken during 2017 (2 months) and 2018 (4–5 months). Changes in muon tomographic images were linked to visually observable volcanic processes.

(continued on next page)

Table 3 (continued)

Authors	Muon detector	Location	Summary
<i>Glaciology</i>			
Nishiyama et al. (2017)	ECC	Jungfrau region, Bern, Switzerland	3D tomographic images of the bedrock-ice interface were produced and used to infer the stability of the rock mass above in light of the gradual melting of the glaciers. Observation duration was 3 months. This survey took muon flux measurements during a total period of 6 months. A 3D model of the glacier bedrock was reconstructed, and its geometry was linked to possible erosion processes that dominate in upper glacial regions.
Nishiyama et al. (2019)	ECC	Jungfrau region, Bern, Switzerland	
<i>Caves</i>			
Caffau et al. (1997)	RPC	Grotta Gigante, Trieste, Italy	The measurement results of the atmospheric muon flux were used to determine the shape of the cave vault. For comparison, available gravity measurements and digital elevation models were considered. The data acquisition timeframe is stated to be at least 24 h. This study presents a nice assembly of various test sites, where muon flux measurements were performed. Another, projection-based, approach of 3D visualization was taken to present the results.
Oláh et al. (2012)	Closed cathode chamber (see Barnaföldi et al., 2012)	Various caves around Budapest, Hungary	
<i>Fault zones</i>			
Tanaka et al. (2011)	Scintillator	Itoigawa-Shizuoka Tectonic Line (ISTL), Itoigawa, Japan	Use of 2D muon tomographic imaging to locate a low-density, i.e. highly fractured, zone parallel to the ISTL and identification thereof as a possible new fault. A correlation between water content (i.e. rainfall) and muon attenuation was observed, which strengthened this implication. The authors present an approach to perform a 3D inversion based on a voxel parametrisation of a geologically well-known section. A low-density zone in one geologic unit was interpreted as a karstic network, that was able to form due to the presence of localised fault zones.
Lesparre et al. (2017)	Scintillator	Tournemire, Aveyron, France	
<i>Borehole applications</i>			

Table 3 (continued)

Authors	Muon detector	Location	Summary
Oláh et al. (2018)	Closed cathode chamber (see Barnaföldi et al., 2012)	NEC Tamagawa Plant, Kanagawa, Japan	In this study the muon detector was deployed in a vertical borehole for the imaging of a near concrete pillar. Images were produced at different total measurement lengths (up to 2 weeks).
Bonneville et al. (2019)	Scintillator	Los Alamos Canyon, New Mexico, USA	A borehole detector (horizontal borehole) was tested against a large-scale detector in a nearby tunnel. It was shown that small-scale borehole detectors may prove useful if accessibility below the target is not given.
<i>Geophysical exploration</i>			
Bryman et al. (2014)	Scintillator	Nyrstar Myra Falls mine, British Columbia, Canada	In this book chapter a case study is presented where the authors applied a muon detector inside a mine, where a known ore body is located between tunnel and surface. The collected muon data was compared to ample existing borehole data and a good agreement was found in the two different inversions.
Baccani et al. (2019)	Scintillator	San Silvestro Archaeo-Mining Park, Tuscany, Italy	A 53-day measurement campaign was conducted in an abandoned mine. There, a high-resolution image of the rock space above was made, thereby locating previously unknown cavities and a high-density vein.

3) Accessibility (Location): “Is there a suitable place to deploy a muon detector?”

If the technology can be applied to the researcher's problem, the issue of accessibility has to be solved next. As we have mentioned above, muon tomography requires the detector to be located underneath the study object (e.g., Fig. 1). This is the case because one measures muons that originate from the natural cosmic ray flux, i.e. from above. This implies that the study object must either be topographically distinct (like a volcano) or accessible from underneath (for example caves, mines and tunnels), a circumstance that might be considered one of the greatest limitations of muon tomography. As can be seen in Ch. 3, researchers have already begun to examine whether borehole muon detectors can be used, which might prove a suitable solution for future applications. In every case one has to remember that muon tomography remains a shallow subsurface imaging technique, meaning that when the overburden is larger than ~1 km, reliable results are difficult to obtain (see Ch. 4.2 for more details on this).

4) Accessibility (Technology): “Is there a physics institute nearby that can provide detectors and know-how?”

We stated earlier that the know-how of particle detection (i.e. detector construction and analysis) is still very much concentrated in the (particle) physics community. Unless this changes, most prospective

muon tomography experiments will typically require the collaboration with a particle physics institute.

4.2. Operation phase

Whereas Ch. 4.1 focused on the issues during the planning of an experimental campaign, we like to discuss here some central problems that appear once the decision has been taken to use muon tomography. Usually, these questions revolve around some technical aspects that are nevertheless important to consider.

5) Detectors: “Which detector should I use?”

As explained in Ch. 2.4, there are a lot of muon detector variants to choose from. In reality, this choice is smaller due to the availability of the know-how and hardware at the collaborating physics institute (i.e. not every physics lab possesses a dedicated emulsion analysis infrastructure). Thus, it is a viable strategy to think about the deployment conditions and the instrumental specifics that a muon detector should encompass. For example, it would make no sense to deploy a detector inside a tunnel for a long time without any power supply or a nuclear emulsion in conditions that exhibit large temperature changes over the measurement period. As particle detectors are very often custom made, they can also be designed to operate in the desired environment. Therefore, one is best advised to discuss this matter within the collaboration and elaborate a roadmap.

A problem that is always tied to the choice of the detector is the issue of how much material has to be transported to the measurement location. We have to inform the reader at this point that depending on the size of the detector (e.g. due to a low flux because one measures underground) and the amount of additional shielding (shielding materials are always high density, like lead) may blow up the total weight of the equipment. Thus, we want to stress the importance of planning the logistics sufficiently early in the project. However, the amount of equipment severely depends on the goal of the measurement, type of detector, location, etc. As it is difficult to provide the reader with a generally valid estimation of how much material is needed, we recommend discussing this point with the detector experts within the collaboration. Another

good practice would be to gain an overview of the detectors and material that other groups in similar situations have used (see Ch. 3 as a starting point).

6) Exposure: “How long do I need to collect muons until I get useful results?”

In the course of the experimental planning, it is of utmost importance to have a rough idea of how long the data acquisition will take until the processing of data can start, such that subsequent project steps can be scheduled. In order to answer this, a back-of-the-envelope calculation is usually enough. We quickly show how this can be read of a chart that was produced for addressing this point. Interested readers are also referred to Appendix E, where we elucidate the rationale behind this approach.

The aforementioned chart is depicted in Fig. 11 as a series of straight lines in a log-log plot. Every line denotes another relative spatial resolution (1%, 5%, 10%, 20%). Users usually have already a target spatial resolution in mind before deciding on the exposure parameters (i.e. exposure time and detector area). The chart can be used by first deciding, on which spatial resolution the experiment should have and then deciding on the detector size (i.e. area) and the exposure time. The resulting point in the graph should lie in the vicinity of the chosen spatial resolution line. This is nothing else as the trade-off between detector area and exposure time, i.e. the longer one records the muon flux, the smaller the detector can be, in order to record a muon flux of equal statistical significance.

As this sounds very technical, we included in Fig. 11 a small example from our own experimental campaign (Nishiyama et al., 2019). In that study we had three operating detector sites, where the thickness of the overlying rock units was roughly 600 m (i.e. distance from the detector to the middle of the surface of the study object; in our case this was the base of a glacier). We were targeting a relative spatial resolution of 10%, which corresponds to an absolute spatial resolution of around 60 m. Please note, that this value is the lateral spatial resolution, i.e. perpendicular to the viewing direction and not along it. This can also be understood as the bin size that one plans on using during the data processing. Limited by the total scanning throughput of our

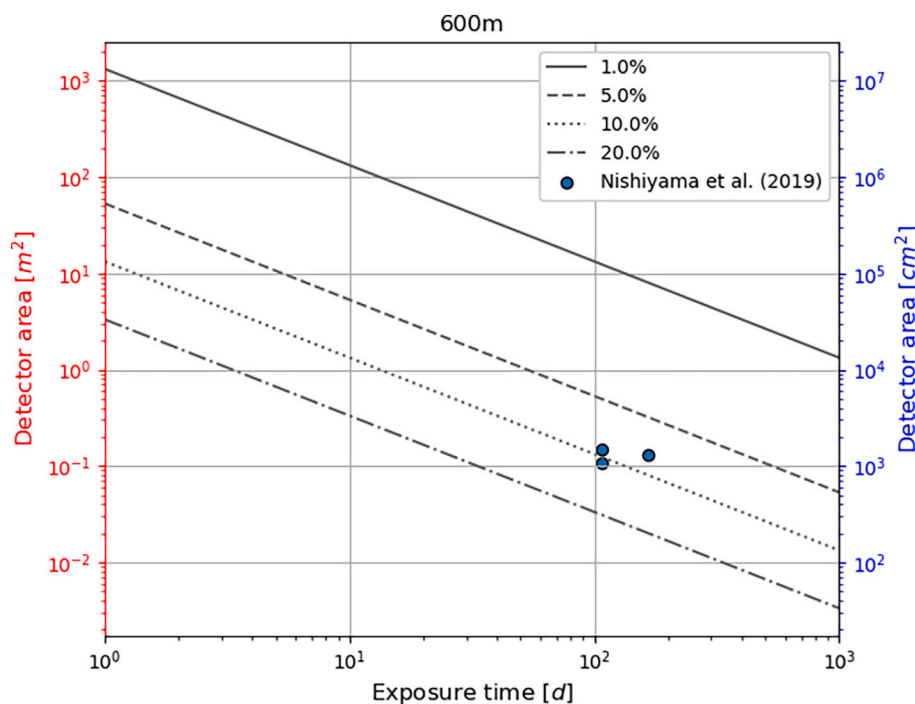


Fig. 11. Decision help chart for the two experimental parameters, i.e., the detector size and the exposure time, in case of 600 m of rock that overlie the detector site (e.g. Fig. 1). Parallel lines indicate the amount of desired lateral precision one can achieve by using a corresponding area/time-point. The three blue dots represent an example from an earlier study performed on a glacier (Nishiyama et al., 2019). (For interpretation of the references to colour in this figure legend, the reader is referred to the web version of this article.)

infrastructure, the $0.1 \text{ m}^2 - 0.2 \text{ m}^2$ were an upper boundary to the overall detector size. Thus, we settled with an exposure time of around 100 d – 200 d.

In Appendix E, we provide the prospective user with similar plots as Fig. 11 but for different expected thicknesses of rocks above the detector site. Alternatively, the reader may use the respective formulae to plot his/her own version of this graph.

7) Placement: “Where should I position my detectors?”

This question relates somewhat to point 3 in the previous chapter (4.1) where we discussed the physical accessibility of the measurement location. First, it is important that the detector is located below the target, in order to detect the natural cosmic ray muons. Another issue that should be considered from an experimental design point of view is the arrangement of different detectors with respect to each other. Frankly, if a 3D muon tomography is the aim, one is advised to distribute the detectors as much as possible around the object in question. This could help prevent somewhat against an underdetermined inverse problem, where individual parameters cannot be resolved well because the detector geometry only allows to gain information on the correlation between the parameters and not their absolute values.

8) Synergies: “Can I improve my results by means of other geophysical methods?”

This last issue ties strongly to point 2 from the previous chapter (4.1). Namely, the question if other geophysical methods are better suited to fill the needs of the researcher. Here, we change the perspective on that question slightly and ask if there are other geophysical methods that may reinforce the muon tomography measurements. Many of the examples given in Ch. 3 are studies that utilise gravimetry in addition to muon tomography. This is a natural choice, as both methods are sensitive to the same physical parameter, i.e. material density. Additionally, both methods compensate many weaknesses of the respective other. This yields an ideal synergy between these methods. It may at this point also be useful to consult fellow geoscientists who are experienced in geophysical imaging methods to get an idea if they are compatible with muon tomography.

9) Analysis: “Do muons always travel in a straight way?”

The short answer to this question is in general no as the chapter about multiple coulomb scattering (2.3.3) has explained. However, the instances where the mentioned scattering becomes important are usually rare (see Fig. 5c, where only the directions near the outline of the mountain are affected). Consequently, for the majority of directions, the muon tracks can be considered straight. This has serious implications for

the inversion, as then a density-length approach can be chosen, which would correspond to a ray theory approach in seismology.

5. Conclusions

Until now researchers have mostly utilised well-established geophysical methods such as seismic tomography, electric resistivity tomography, ground penetrating radar and others to gain insights into the Earth’s interior. In recent years a new method originating from particle physics, muon tomography, has been used more frequently to collect data on geological features at a few tens to hundreds of meters distance to the surface. This new technology synergises well with the established geophysical methods as their advantages and drawbacks balance each other. Muon tomography offers the possibility to measure structural properties (like the density distribution) within the object in question, while not having to go near dangerous or inaccessible places. Naturally, there are also scenarios where the established geophysical methods yield much better results. One of the most serious limitations of muon tomography, for example, is the fact that detectors always have to be placed below the target and can only inspect the material above.

To be able to take the decision whether this new technology might be useful for one’s research, well-founded knowledge on the possibilities and limitations of muon tomography is needed. However, the know-how on this technology is in most cases located in particle physics laboratories. With this work, we present a starting point for prospective users with a geoscientific background to become familiar with muon tomography. The summaries of important aspects should help interested readers to form a solid overview.

The aspects in the previous chapters are not meant to be exhaustive. They consist, however, of a few important cornerstones that we think are important to get an idea on the whole topic of muon tomography. The guidelines are also intended to point the prospective users into the right direction. The showcase of different applications is thought to be an inspiration for readers. Knowing about the potential uses of muon tomography, one can employ this technology in their own research field. The possible applications of this technology are still far from exhausted.

Declaration of Competing Interest

The authors declare that they have no known competing financial interests or personal relationships that could have appeared to influence the work reported in this paper.

Acknowledgements

We thank the Swiss National Science Foundation (project No 159299 awarded to F. Schlunegger and A. Ereditato) for their financial support of this research project.

Appendix A. Cosmic ray flux models

A.1. Flux model description

A.1.1. Tang model (modified Gaisser model)

The basic analytical muon flux model that one learns when working with muons originating from cosmic rays can be found in Eq. 29.4 of Tanabashi et al., (2018, p. 426), which reads

$$\frac{d\Phi_G}{dE}(E\theta) = 0.14E^{-2.7} \left\{ \frac{1}{1 + \frac{1.1E\cos(\theta)}{115 \text{ GeV}}} + \frac{0.054}{1 + \frac{1.1E\cos(\theta)}{850 \text{ GeV}}} \right\} \quad (\text{A1})$$

This may be interpreted as a term that describes the production of muons from decaying pions and kaons, where both values are multiplied by an overall scaling factor. Here E denotes the muon’s energy and θ is the incidence angle relative to the zenith. The exact derivation of Eq. (A1) can be found in Gaisser et al. (2016), which is acknowledged by the subscript G in Φ_G . This simplified model already reproduces the muon flux quite well (see

Fig. 29.5 in [Tanabashi et al., 2018](#)). However, because the agreement between model and measurements worsens especially in the low energy region, several modifications as well as other model parametrisations have been proposed. In this context, [Tang et al. \(2006\)](#) introduced a slight modification of the ‘‘Gaisser equation’’ (A2), to account for this issue:

$$\frac{d\Phi_{\Gamma}}{dE}(E\theta) = A * 0.14 E^{-2.7} \left\{ \frac{1}{1 + \frac{1.1 E \cos(\theta^*)}{115 \text{ GeV}}} + \frac{0.054}{1 + \frac{1.1 E \cos(\theta^*)}{850 \text{ GeV}}} + r_c \right\} \quad (\text{A2})$$

Here the necessary additional parameters are given by

$$r_c = 10^{-4} \quad (\text{A3})$$

$$\Delta = 2.06 * 10^{-3} * \left(\frac{950}{\cos(\theta^*)} - 90 \right) \quad (\text{A4})$$

$$\tilde{E} = E + \Delta \quad (\text{A5})$$

$$A = 1.1 * \left(\frac{90 \sqrt{\cos(\theta)} + 0.001}{1030} \right)^{\frac{4.5}{\cos(\theta^*)}} \quad (\text{A6})$$

where

$$\cos(\theta^*) = \sqrt{\frac{x^2 + p_1^2 + p_2 x^{p_3} + p_4 x^{p_5}}{1 + p_1^2 + p_2 + p_4}} \quad (\text{A7})$$

and the muon energy E is substituted by

$$E \rightarrow \frac{3E + \frac{7}{\cos(\theta^*)}}{10} \quad (\text{A8})$$

if it fulfils the inequality $E \leq 1/\cos(\theta^*)$ GeV. The parameters in Eq. (A7) are $x = \cos(\theta)$, $p_1 = 0.102573$, $p_2 = -0.068287$, $p_3 = 0.958633$, $p_4 = 0.0407253$ and $p_5 = 0.817285$.

A.1.2. Reyna-Bugaev model

A second muon flux model is given by [Bugaev et al. \(1998\)](#) who proposed an empirical fitting formula to the muon flux measurements at sea level for vertical (i.e. zenith angle $\theta = 0^\circ$) incident muons. The related equation is given by

$$\frac{d\Phi_{\text{B}}}{dE}(E) = C * p^{-(\gamma_0 + \gamma_1 \log_{10}(p) + \gamma_2 \log_{10}^2(p) + \gamma_3 \log_{10}^3(p))} \quad (\text{A9})$$

where $p \equiv p(E)$ is the momentum of the muon in GeV c^{-1} . This is related to the muon energy by the relativistic energy-momentum relation:

$$p^2 c^2 = E^2 - m_\mu^2 c^4 \quad (\text{A10})$$

In Eq. (13), m_μ denotes the rest mass of the muon, which equals 0.10566 GeV c^{-2} . The gamma parameters in Eq. (A9) include different values for different ranges of momentum and can be looked up in Table II of [Bugaev et al. \(1998\)](#). Attentive readers have realised that Eq. (A9) does not have any zenith angle dependency. This shortcoming of the model has been accounted for by [Reyna \(2006\)](#) by modifying Eq. (A9) by

$$\frac{d\Phi_{\text{RB}}}{dE}(E\theta) = \tilde{C} * \tilde{p}^{-\left(\tilde{\gamma}_0 + \tilde{\gamma}_1 \log(\tilde{p}) + \tilde{\gamma}_2 \log^2(\tilde{p}) + \tilde{\gamma}_3 \log^3(\tilde{p})\right)} * \cos^3(\theta) \quad (\text{A11})$$

where

$$\tilde{p} = p * \cos(\theta) \quad (\text{A12})$$

with p taken from Eq. (A10). The tilde parameters in Eq. (A11) have been re-evaluated by [Reyna \(2006\)](#) to $\tilde{C} = 0.00253$, $\tilde{\gamma}_0 = 0.2455$, $\tilde{\gamma}_1 = 1.288$, $\tilde{\gamma}_2 = -0.2555$ and $\tilde{\gamma}_3 = 0.0209$ respectively. The subscript RB stands for Reyna-Bugaev.

A.1.3. Reyna-Hebbeker model

A third model was presented by [Hebbeker and Timmermans \(2002\)](#). It is empirical in nature, very similar to the Bugaev model described above, and it follows a power law relationship as well,

$$\frac{d\Phi_{\text{H}}}{dE}(E) = C * 10^{H(y)} \quad (\text{A13})$$

Here, $y = \log_{10}(p)$, with again p from Eq. (A10) and

$$H(y) = H_1 \left(\frac{y^3}{2} - \frac{5y^2}{2} + 3y \right) + H_2 \left(-\frac{2y^3}{3} + 3y^2 - \frac{10y}{3} + 1 \right) + H_3 \left(\frac{y^3}{6} - \frac{y^2}{2} + \frac{y}{3} \right) + S_2 \left(\frac{y^3}{3} - 2y^2 + \frac{11y}{3} - 2 \right) \quad (\text{A14})$$

The parameters in Eq. (A14) have been fitted to $C = 0.86$, $H_1 = 0.133$, $H_2 = -2.521$, $H_3 = -5.78$ and $S_2 = -2.11$. Following Lesparre et al. (2010), we may supplement this pure zenith muon flux with an expression that describes an angle dependency, similar to the way as has been done with Eq. (A11). The resulting RH, i.e. Reyna-Hebbeker, flux is written as

$$\frac{d\Phi_{\text{RH}}}{dE}(E\theta) = C * 10^{H(\tilde{y})} * \cos^3(\theta) \quad (\text{A15})$$

with

$$\tilde{y} = \log_{10}(p^* \cos(\theta)) \quad (\text{A16})$$

A.1.4. Sato model

The last model that we present here is the one described by Sato (2016), which we address from here onwards as $d\Phi_S/dE$. This model is based on a Monte Carlo Simulation in the particle transport framework PHITS (Sato et al., 2013). Two variants are available for users who are interested in adapting this model into their calculations. These variants are either what is referred to as EXPACS, which lets the user calculate the (among other particles) muon flux by an Excel spreadsheet, or a more involved one, referred to as PARMA, where the user alters the input files of the model itself. In both cases the user is returned a list of energy vs. muon flux. Table A1 shows the calculated muon flux at Bern, Switzerland (Lat: 46.94°N, Lon: 7.44°E) at sea level (see Ch. 2.2.3 on information on how to incorporate height information) for the three different zenith angles $\theta = 0^\circ, 45^\circ, 60^\circ$.

Table A1
Numerical results from PARMA (Sato, 2016) for the location of Bern, Switzerland (Lat: 46.94°N, Lon: 7.44°E) for an altitude of 0 m above sea level.

Total energy E [GeV]	Differential muon flux $\frac{d\Phi_S}{dE}$ [$\text{GeV}^{-1}\text{m}^{-2}\text{s}^{-1}\text{sr}^{-1}$]		
	$\theta = 0^\circ$	$\theta = 45^\circ$	$\theta = 60^\circ$
1.13	2.12E-03	5.93E-04	2.39E-04
1.42	1.80E-03	5.36E-04	2.29E-04
1.79	1.49E-03	4.73E-04	2.15E-04
2.25	1.19E-03	4.05E-04	1.97E-04
2.84	9.23E-04	3.36E-04	1.74E-04
3.57	6.90E-04	2.69E-04	1.48E-04
4.50	4.97E-04	2.06E-04	1.21E-04
5.66	3.45E-04	1.52E-04	9.41E-05
7.13	2.31E-04	1.07E-04	6.98E-05
8.97	1.49E-04	7.25E-05	4.93E-05
11.29	9.30E-05	4.70E-05	3.31E-05
14.22	5.62E-05	3.10E-05	2.30E-05
17.90	3.30E-05	1.99E-05	1.55E-05
22.54	1.88E-05	1.24E-05	1.01E-05
28.37	1.05E-05	7.52E-06	6.32E-06
35.72	5.68E-06	4.42E-06	3.83E-06
44.97	3.01E-06	2.52E-06	2.25E-06
56.61	1.56E-06	1.40E-06	1.29E-06
71.26	7.91E-07	7.49E-07	7.12E-07
89.72	3.93E-07	3.93E-07	3.85E-07
112.94	1.95E-07	2.05E-07	2.07E-07
142.19	9.72E-08	1.07E-07	1.11E-07
179.01	4.80E-08	5.48E-08	5.93E-08
225.36	2.35E-08	2.79E-08	3.12E-08
283.71	1.14E-08	1.40E-08	1.63E-08
357.17	5.12E-09	6.42E-09	7.73E-09
449.65	2.26E-09	2.88E-09	3.58E-09
566.08	9.93E-10	1.28E-09	1.62E-09
712.64	4.35E-10	5.59E-10	7.25E-10
897.16	1.90E-10	2.42E-10	3.19E-10
1129.40	8.32E-11	1.05E-10	1.39E-10
1421.90	3.62E-11	4.56E-11	6.06E-11
1790.10	1.58E-11	1.99E-11	2.64E-11
2253.60	6.87E-12	8.64E-12	1.15E-11
2837.10	2.99E-12	3.76E-12	4.99E-12
3571.70	1.30E-12	1.63E-12	2.17E-12
4496.50	5.63E-13	7.09E-13	9.41E-13
5660.80	2.45E-13	3.08E-13	4.09E-13
7126.40	1.06E-13	1.34E-13	1.77E-13
8971.60	4.60E-14	5.80E-14	7.69E-14

A.2. Muon flux uncertainty estimates for higher zenith angles

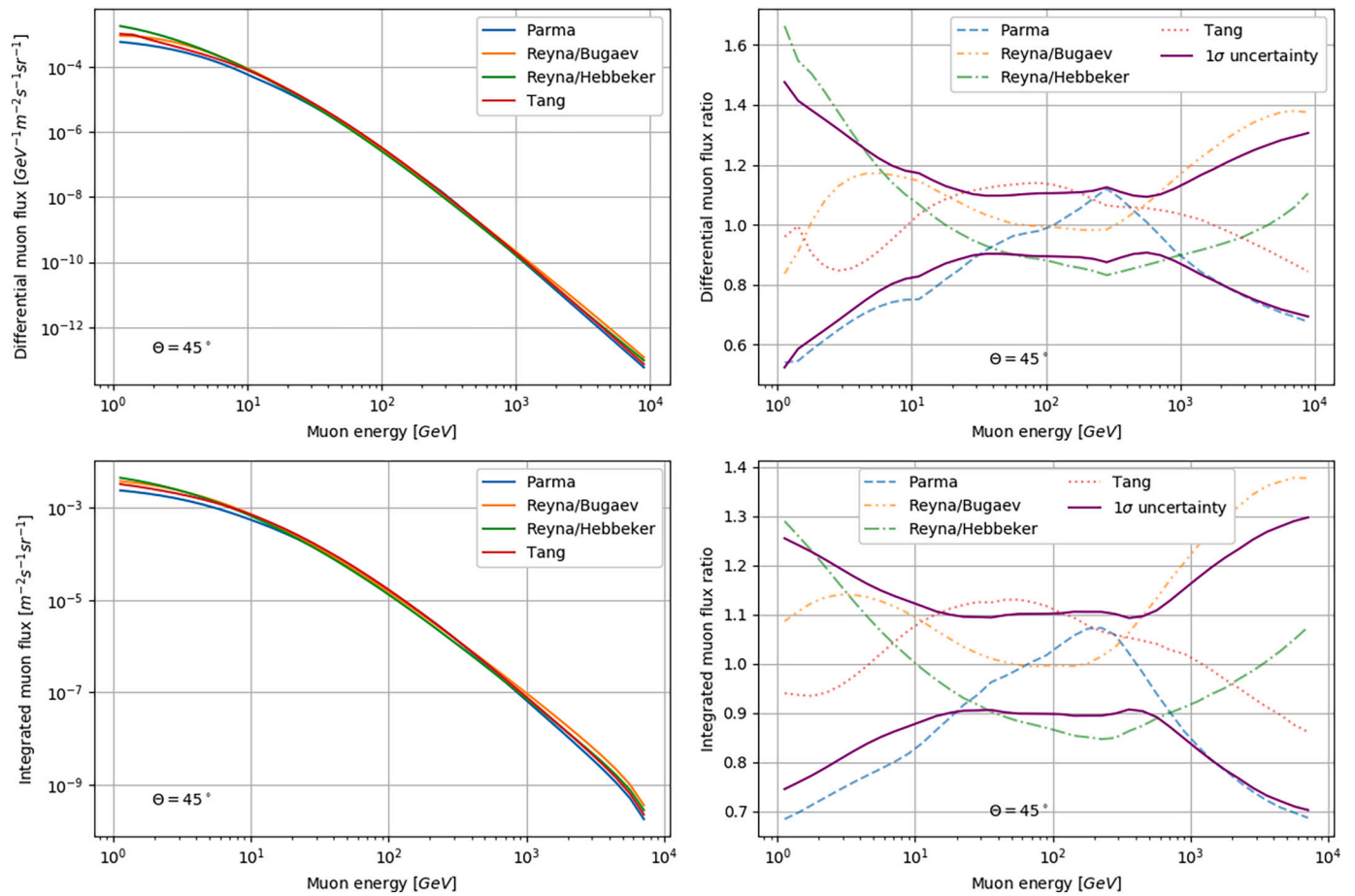


Fig. A1. Comparison of the four muon flux models (see Appendix A1.1 – A1.4) including an uncertainty estimate for a zenith angle of $\theta = 45^\circ$. *Top left:* Differential muon flux as a function of energy. *Top right:* Differential muon flux ratio to the mean differential flux $\langle d\Phi/dE \rangle$ (see Eq. 5). *Bottom left:* Integrated muon flux as a function of the lower integration boundary (i.e. E_{cut} in Eq. 4). *Bottom right:* Integrated muon flux ratio to the mean integrated flux $\langle \Phi \rangle$. The 1σ -uncertainty in the right-hand side plots has been calculated according to Eqs. (6) & (7).

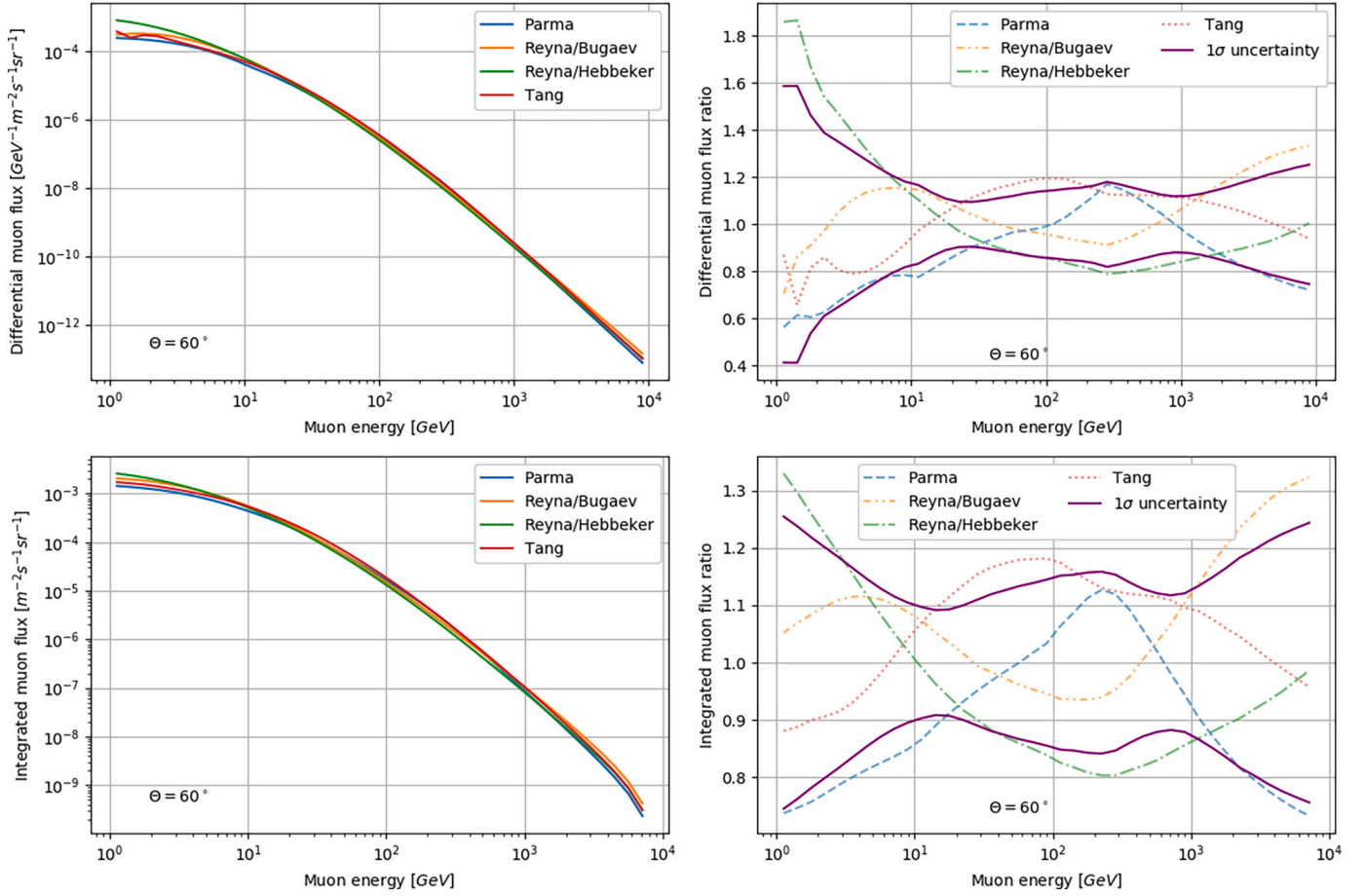


Fig. A2. Comparison of the four muon flux models (see Appendix A1.1 – A1.4) including an uncertainty estimate for a zenith angle of $\theta = 60^\circ$. *Top left:* Differential muon flux as a function of energy. *Top right:* Differential muon flux ratio to the mean differential flux ($d\Phi/dE$) (see Eq. 5). *Bottom left:* Integrated muon flux as a function of the lower integration boundary (i.e. E_{cut} in Eq. 4). *Bottom right:* Integrated muon flux ratio to the mean integrated flux (Φ). The 1σ -uncertainty in the right-hand side plots has been calculated according to Eqs. (6) & (7).

Appendix B. Energy loss tables

The energy loss tables, as mentioned in Ch. 2.3.2 may be found on the website of the Particle Data Group, the international collaboration of particle physicists (<https://pdg.lbl.gov/> → Atomic & Nuclear Properties). They offer energy loss tables for every pure element as well as for selected compounds. As an example, we present the table for “standard rock”, reduced only to the most important information. Please note that in Table B1 the indicated energy is the kinetic energy of the muon, T and not the total energy, E . They are however related by the formula

$$T = E - E_\mu \quad (\text{B1})$$

where $E_\mu = 105.7$ MeV is the rest mass of the muon. For $E \gg E_\mu$ we have $E \approx T$.

Table B1

Excerpt from the energy loss table for standard rock between 1GeV – 900 GeV. T denotes the kinetic energy of the muon (Eq. B1), dE/dx is the energy loss from Eq. (11), and R refers to the penetration range from Eq. (13).

T [MeV]	dE/dx [MeV cm ² g ⁻¹]	R [g cm ⁻²]	T [MeV]	dE/dx [MeV cm ² g ⁻¹]	R [g cm ⁻²]
1.000E+03	1.808E+00	5.534E+02	1.000E+05	2.747E+00	4.084E+04
1.200E+03	1.837E+00	6.631E+02	1.200E+05	2.837E+00	4.800E+04
1.400E+03	1.862E+00	7.712E+02	1.400E+05	2.925E+00	5.495E+04
1.700E+03	1.895E+00	9.309E+02	1.700E+05	3.057E+00	6.498E+04
2.000E+03	1.922E+00	1.088E+03	2.000E+05	3.187E+00	7.459E+04
2.500E+03	1.960E+00	1.346E+03	2.500E+05	3.400E+00	8.977E+04
3.000E+03	1.990E+00	1.599E+03	3.000E+05	3.611E+00	1.040E+05
3.500E+03	2.016E+00	1.848E+03	3.500E+05	3.824E+00	1.175E+05
4.000E+03	2.038E+00	2.095E+03	4.000E+05	4.037E+00	1.302E+05
4.500E+03	2.058E+00	2.339E+03	4.500E+05	4.250E+00	1.423E+05
5.000E+03	2.075E+00	2.581E+03	5.000E+05	4.465E+00	1.538E+05
5.500E+03	2.091E+00	2.821E+03	5.500E+05	4.677E+00	1.647E+05
6.000E+03	2.105E+00	3.059E+03	6.000E+05	4.890E+00	1.752E+05

(continued on next page)

Table B1 (continued)

T [MeV]	dE/dx [MeV cm ² g ⁻¹]	R [g cm ⁻²]	T [MeV]	dE/dx [MeV cm ² g ⁻¹]	R [g cm ⁻²]
7.000E+03	2.130E+00	3.531E+03	7.000E+05	5.318E+00	1.948E+05
8.000E+03	2.152E+00	3.998E+03	8.000E+05	5.748E+00	2.129E+05
9.000E+03	2.171E+00	4.461E+03	9.000E+05	6.180E+00	2.296E+05
1.000E+04	2.188E+00	4.920E+03	1.000E+06	6.615E+00	2.453E+05
1.200E+04	2.218E+00	5.827E+03	1.200E+06	7.475E+00	2.737E+05
1.400E+04	2.244E+00	6.724E+03	1.400E+06	8.340E+00	2.990E+05
1.700E+04	2.277E+00	8.051E+03	1.700E+06	9.647E+00	3.324E+05
2.000E+04	2.306E+00	9.360E+03	2.000E+06	1.096E+01	3.616E+05
2.500E+04	2.347E+00	1.151E+04	2.500E+06	1.314E+01	4.032E+05
3.000E+04	2.383E+00	1.362E+04	3.000E+06	1.533E+01	4.384E+05
3.500E+04	2.416E+00	1.571E+04	3.500E+06	1.754E+01	4.688E+05
4.000E+04	2.447E+00	1.776E+04	4.000E+06	1.976E+01	4.957E+05
4.500E+04	2.476E+00	1.979E+04	4.500E+06	2.198E+01	5.197E+05
5.000E+04	2.503E+00	2.180E+04	5.000E+06	2.422E+01	5.413E+05
5.500E+04	2.530E+00	2.379E+04	5.500E+06	2.643E+01	5.611E+05
6.000E+04	2.556E+00	2.575E+04	6.000E+06	2.865E+01	5.792E+05
7.000E+04	2.606E+00	2.963E+04	7.000E+06	3.311E+01	6.117E+05
8.000E+04	2.654E+00	3.343E+04	8.000E+06	3.759E+01	6.400E+05
9.000E+04	2.701E+00	3.717E+04	9.000E+06	4.208E+01	6.651E+05

Appendix C. Radiation length of a real rock

In this chapter we guide the reader through an exemplary calculation from the raw XRF measurements to a radiation length.

We start off by showing the raw XRF data that was collected during our measurement campaign for [Nishiyama et al. \(2017\)](#) in [Table C1](#).

Table C1

Raw XRF measurement data taken during the muon tomography measurement campaign of [Nishiyama et al. \(2017\)](#). Data in columns denote weight percent oxide fractions.

Sample	1	2	3	4	5	6	7	8	9	10	11	12	13
Oxide													
SiO ₂	0.6131	0.5981	0.6997	0.6139	0.6201	0.6401	0.5691	0.6555	0.7101	0.7181	0.6287	0.7593	0.6771
TiO ₂	0.0123	0.0067	0.0076	0.0094	0.0084	0.0088	0.0156	0.0089	0.0069	0.0065	0.0075	0.0055	0.0083
Al ₂ O ₃	0.1567	0.1873	0.1481	0.1921	0.178	0.1736	0.1875	0.1719	0.1394	0.1455	0.1902	0.1142	0.147
Fe ₂ O ₃	0.087	0.0791	0.0496	0.0686	0.065	0.0586	0.0833	0.0648	0.0486	0.0428	0.0683	0.0303	0.0558
MnO	0.001	0.0012	0.0009	0.0009	0.0008	0.0008	0.0011	0.0009	0.0007	0.0006	0.0009	0.0005	0.0009
MgO	0.0359	0.0285	0.0206	0.0288	0.0254	0.0246	0.0318	0.0215	0.0225	0.0192	0.0266	0.0139	0.0229
CaO	0.0202	0.0071	0.0201	0.0137	0.0147	0.0244	0.0325	0.0146	0.0168	0.0167	0.012	0.0161	0.0125
Na ₂ O	0.0228	0.0248	0.0404	0.0323	0.0369	0.0372	0.0518	0.0442	0.0365	0.0378	0.0451	0.0264	0.0199
K ₂ O	0.0343	0.0465	0.0287	0.0469	0.0465	0.0406	0.0315	0.0354	0.0233	0.0282	0.0452	0.0223	0.031
P ₂ O ₅	0.0041	0.0029	0.0021	0.0027	0.0035	0.0064	0.0123	0.0014	0.0016	0.003	0.0014	0.0019	0.0009
Sum	0.9874	0.9822	1.0178	1.0093	0.9993	1.0151	1.0165	1.0191	1.0064	1.0184	1.0259	0.9904	0.9763

Following Appendix B2 of [Lechmann \(2021\)](#) we may rearrange [Table C1](#) into pure element data by decomposing them into their elementary constituent weight fractions. This is shown in [Table C2](#).

Table C2

Raw data from [Table C1](#) decomposed into elementary weight fractions.

Sample	1	2	3	4	5	6	7	8	9	10	11	12	13
Element													
Si	0.2866	0.2796	0.3271	0.2870	0.2899	0.2992	0.2660	0.3064	0.3319	0.3357	0.2939	0.3549	0.3165
Ti	0.0074	0.0040	0.0046	0.0056	0.0050	0.0053	0.0093	0.0053	0.0041	0.0039	0.0045	0.0033	0.0050
Al	0.0829	0.0991	0.0784	0.1017	0.0942	0.0919	0.0992	0.0910	0.0738	0.0770	0.1007	0.0604	0.0778
Fe	0.0609	0.0553	0.0347	0.0480	0.0455	0.0410	0.0583	0.0453	0.0340	0.0299	0.0478	0.0212	0.0390
Mn	0.0008	0.0009	0.0007	0.0007	0.0006	0.0006	0.0009	0.0007	0.0005	0.0005	0.0007	0.0004	0.0007
Mg	0.0216	0.0172	0.0124	0.0174	0.0153	0.0148	0.0192	0.0130	0.0136	0.0116	0.0160	0.0084	0.0138
Ca	0.0144	0.0051	0.0144	0.0098	0.0105	0.0174	0.0232	0.0104	0.0120	0.0119	0.0086	0.0115	0.0089
Na	0.0169	0.0184	0.0300	0.0240	0.0274	0.0276	0.0384	0.0328	0.0271	0.0280	0.0335	0.0196	0.0148
K	0.0285	0.0386	0.0238	0.0389	0.0386	0.0337	0.0261	0.0294	0.0193	0.0234	0.0375	0.0185	0.0257
P	0.0018	0.0013	0.0009	0.0012	0.0015	0.0028	0.0054	0.0006	0.0007	0.0013	0.0006	0.0008	0.0004
O	0.4656	0.4627	0.4909	0.4751	0.4708	0.4808	0.4704	0.4842	0.4893	0.4952	0.4822	0.4913	0.4737
Sum	0.9874	0.9822	1.0178	1.0093	0.9993	1.0151	1.0165	1.0191	1.0064	1.0184	1.0259	0.9904	0.9763

At this point we may normalise the data, i.e. rescale each data column to 1, as depicted in [Table C3](#).

Table C3
Elementary weight fraction data from Table C2 normalised to 1.

Sample	1	2	3	4	5	6	7	8	9	10	11	12	13
Element													
Si	0.2902	0.2846	0.3213	0.2843	0.2901	0.2948	0.2617	0.3007	0.3298	0.3296	0.2865	0.3584	0.3242
Ti	0.0075	0.0041	0.0045	0.0056	0.0050	0.0052	0.0092	0.0052	0.0041	0.0038	0.0044	0.0033	0.0051
Al	0.0840	0.1009	0.0770	0.1007	0.0943	0.0905	0.0976	0.0893	0.0733	0.0756	0.0981	0.0610	0.0797
Fe	0.0616	0.0563	0.0341	0.0475	0.0455	0.0404	0.0573	0.0445	0.0338	0.0294	0.0466	0.0214	0.0400
Mn	0.0008	0.0009	0.0007	0.0007	0.0006	0.0006	0.0008	0.0007	0.0005	0.0005	0.0007	0.0004	0.0007
Mg	0.0219	0.0175	0.0122	0.0172	0.0153	0.0146	0.0189	0.0127	0.0135	0.0114	0.0156	0.0085	0.0141
Ca	0.0146	0.0052	0.0141	0.0097	0.0105	0.0172	0.0229	0.0102	0.0119	0.0117	0.0084	0.0116	0.0092
Na	0.0171	0.0187	0.0294	0.0237	0.0274	0.0272	0.0378	0.0322	0.0269	0.0275	0.0326	0.0198	0.0151
K	0.0288	0.0393	0.0234	0.0386	0.0386	0.0332	0.0257	0.0288	0.0192	0.0230	0.0366	0.0187	0.0264
P	0.0018	0.0013	0.0009	0.0012	0.0015	0.0028	0.0053	0.0006	0.0007	0.0013	0.0006	0.0008	0.0004
O	0.4716	0.4711	0.4823	0.4707	0.4711	0.4736	0.4628	0.4751	0.4862	0.4862	0.4700	0.4961	0.4852
Sum	1.0000	1.0000	1.0000	1.0000	1.0000	1.0000	1.0000	1.0000	1.0000	1.0000	1.0000	1.0000	1.0000

The last step consists of forming so called log-ratios. This means that we divide our rows by one arbitrarily chosen row (we decided on the last row, i.e. oxygen) and take the natural logarithm of the resulting value. See Table C4 for these results.

Table C4
Log-ratios of the values given in Table C3.

Sample	1	2	3	4	5	6	7	8	9	10	11	12	13
$\ln(\text{Si}/\text{O})$	-0.4853	-0.5038	-0.4061	-0.5042	-0.4850	-0.4742	-0.5701	-0.4575	-0.3881	-0.3887	-0.4952	-0.3252	-0.4032
$\ln(\text{Ti}/\text{O})$	-4.1457	-4.7469	-4.6800	-4.4348	-4.5381	-4.5125	-3.9183	-4.5083	-4.7734	-4.8450	-4.6753	-5.0043	-4.5561
$\ln(\text{Al}/\text{O})$	-1.7253	-1.5406	-1.8346	-1.5418	-1.6089	-1.6549	-1.5561	-1.6718	-1.8920	-1.8610	-1.5665	-2.0955	-1.8063
$\ln(\text{Fe}/\text{O})$	-2.0349	-2.1238	-2.6497	-2.2928	-2.3375	-2.4621	-2.0887	-2.3686	-2.6669	-2.8058	-2.3119	-3.1435	-2.4962
$\ln(\text{Mn}/\text{O})$	-6.3989	-6.2103	-6.5572	-6.5245	-6.6331	-6.6541	-6.3139	-6.5434	-6.8053	-6.9713	-6.5393	-7.1459	-6.5214
$\ln(\text{Mg}/\text{O})$	-3.0684	-3.2929	-3.6767	-3.3090	-3.4254	-3.4784	-3.1999	-3.6202	-3.5853	-3.7557	-3.4032	-4.0710	-3.5351
$\ln(\text{Ca}/\text{O})$	-3.4736	-4.5129	-3.5314	-3.8821	-3.8025	-3.3167	-3.0083	-3.8373	-3.7076	-3.7254	-4.0293	-3.7542	-3.9707
$\ln(\text{Na}/\text{O})$	-3.3152	-3.2248	-2.7960	-2.9871	-2.8448	-2.8577	-2.5048	-2.6923	-2.8943	-2.8711	-2.6680	-3.2224	-3.4684
$\ln(\text{K}/\text{O})$	-2.7944	-2.4838	-3.0255	-2.5017	-2.5011	-2.6578	-2.8898	-2.8019	-3.2307	-3.0517	-2.5534	-3.2787	-2.9127
$\ln(\text{P}/\text{O})$	-5.5615	-5.9015	-6.2834	-5.9995	-5.7308	-5.1482	-4.4732	-6.6751	-6.5522	-5.9354	-6.6710	-6.3844	-7.0950
$\ln(\text{O}/\text{O})$	0.0000	0.0000	0.0000	0.0000	0.0000	0.0000	0.0000	0.0000	0.0000	0.0000	0.0000	0.0000	0.0000

As these log-ratios are usually statistically well-behaved, i.e. Gaussian-like, we may form a meaningful mean log-ratio of our different samples. For an explanation why this works, the reader is referred to the textbook of Aitchison (1986). Normality plots of this data may additionally be found in Lechmann (2021).

Now we may calculate the mean of the data in Table C4 (see Table C5 for results). By using the back transformation from log-ratios to element weight fractions, i.e.

$$w_{\text{ele},i}^{\text{cle}} = \frac{\exp(r_i)}{1 + \sum_{j=1}^{N_{\text{ele}}-1} \exp(r_j)} \quad (\text{C1})$$

for the numerator elements and

$$w_{\text{ele},N_{\text{ele}}}^{\text{cle}} = \frac{1}{1 + \sum_{j=1}^{N_{\text{ele}}-1} \exp(r_j)} \quad (\text{C2})$$

for de denominator element (oxygen) we can reconstruct meaningful element weight fractions (see Table C6). Once we have these weight fractions, we may perform a weighted average over the inverse values of the radiation length (see Eq. 17) to get the radiation length of our rock. We eventually end up with $1/\Lambda_{0, \text{rock}} = 0.0389 \text{ cm}^2 \text{ g}^{-1}$ or equivalently, $\Lambda_{0, \text{rock}} = 25.72 \text{ g cm}^{-2}$.

With the log-ratio formalism it is theoretically also possible to calculate an error on this radiation length. As this, however, goes too far for the purpose of this calculation, we omit this step.

Table C5
Mean values of the 13 log-ratios given in Table C4.

Log-ratio	Mean value
$\ln(\text{Si}/\text{O})$	-0.4528
$\ln(\text{Ti}/\text{O})$	-4.5645
$\ln(\text{Al}/\text{O})$	-1.7197
$\ln(\text{Fe}/\text{O})$	-2.4448
$\ln(\text{Mn}/\text{O})$	-6.6014
$\ln(\text{Mg}/\text{O})$	-3.4939
$\ln(\text{Ca}/\text{O})$	-3.7348

(continued on next page)

Table C5 (continued)

Log-ratio	Mean value
$\ln(\text{Na}/\text{O})$	-2.9498
$\ln(\text{K}/\text{O})$	-2.8218
$\ln(\text{P}/\text{O})$	-6.0316
$\ln(\text{O}/\text{O})$	0.0000

Table C6

Back-transformed mean values from Table C5. Additionally, the inverse value of the radiation length is also shown. $1/\Lambda_0$ has been calculated according to Eqs. (18) & (19) and Table 1.

Element	Wt-mean	$1/\Lambda_0$ (rad. length) [$\text{cm}^2 \text{g}^{-1}$]
Si	0.3054	0.0458
Ti	0.0050	0.0619
Al	0.0860	0.0416
Fe	0.0417	0.0723
Mn	0.0007	0.0683
Mg	0.0146	0.0399
Ca	0.0115	0.0619
Na	0.0251	0.0361
K	0.0286	0.0578
P	0.0012	0.0472
O	0.4803	0.0292

Appendix D. How to tackle the horizontal offset in multiple coulomb scattering

In this appendix we try to illustrate how we can apply the concepts from Ch. 2.3.3 to an example experimental setup in order to understand how we can cope with the potential out-scattering of particles. Following Tanabashi et al. (2018) we assume that our scattering can be well described by a 2D-Gaussian distribution around zero deviation with a “standard deviation” of $\sigma = \theta_{\text{plane}}$, i.e.

$$p(\theta_x, \theta_y) = \frac{1}{2\pi\theta_{\text{plane}}^2} \exp\left(-\frac{\theta_x^2 + \theta_y^2}{2\theta_{\text{plane}}^2}\right) \quad (\text{D1})$$

An example of how this looks like when this scattering cone hits a detector please see a) of Fig. D1. We see that not all muons hit the detector. However, we also have to account for muons that would not normally hit the detector and are scattered into the detector. We present here a conceptual approach for this non-trivial phenomenon. We may add some imaginary detectors around our real device, which then forms a sort of detector lattice, with one detector being a “unit cell”. For every imaginary detector we can form also such a muon scattering cone, coming from the same direction as the original one (i.e. they are parallel to each other). Muons that would normally not hit this imaginary detector, will instead hit our real detector (at least on the side where real and imaginary detectors touch). These particles are then scattered into our detector (see b) of Fig. D1). This is valid for every point on our detector; c) & d) of Fig. D1 depict the situation for a non-centred point on the detector.

One sees that out-scattering and in-scattering are always balanced and thus the measured muon flux can be reliably measured. One warning has to be made though. If we have to deal with in- and out-scattering, we actually lower the spatial resolution of our measurement. This can be explained by the fact that if we have to rely on imaginary detectors to “catch” our stray muons, then we actively enlarge the effective detector area relative to the structures that we want to observe. In the example from Fig. D1, we tripled the height and width of our detector, meaning that we cannot resolve structures below $\sim 3m$ anymore, as they tend to be “smoothed” out in our measurements. This effect is expected to become even more prominent with lower-energy (i.e. higher scattering angle) muons.

Luckily, as we usually do not use only muons from one energy but from the whole flux (i.e. energy integrated), this “blurring”-effect is usually mitigated to an extent where the blurring is below the resolution one tries to achieve.

Note, that this is only a very rough sketch of the problem and we do not present a definitive solution but only a way on how one might conceptualise this issue. Certainly, more research is needed in this area.

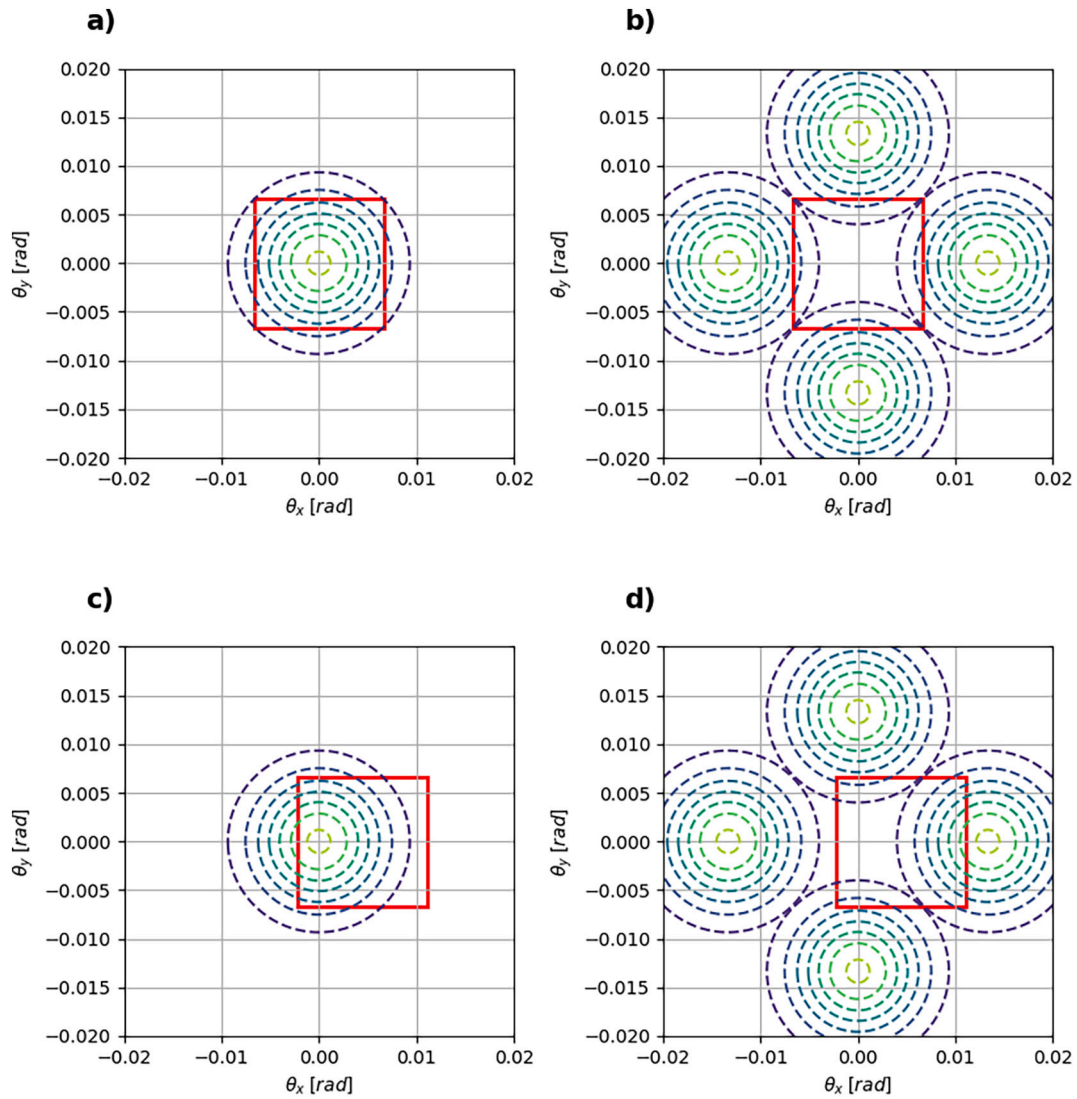


Fig. D1. Examples of out-scattering and in-scattering from different (adjacent) incident muon trajectories on a detector (red rectangle) with side lengths $l = 1$ m. Dashed circles denote the isolines from a 2D Gaussian distribution (here with the parameters for 150m of standard rock and an exit energy of 100GeV; this means $\theta_{\text{plane}} = 4.69\text{mrad}$ (see Table 2)). *a)* A small part of the scattered muons does not hit the detector, i.e. they are scattered “out”. *b)* Scattering-in of muons that would normally not hit the detector. *c)* & *d)* show the same phenomenon if we look at a decentral position on the detector. One can always find a periodic arrangement of detectors to balance in- and out-scattering. (For interpretation of the references to colour in this figure legend, the reader is referred to the web version of this article.)

Appendix E. Derivation of the exposure decision helper

The basis for this derivation is formed by Eq. (4), i.e. the formulation of the integrated flux. However, one does usually not measure the integrated flux directly, but a number of muons, N_{μ} , in a certain solid angle, $\Delta\Omega$, over a certain time, ΔT , on a detector with a definite size, ΔA . Given this description, the relation between the integrated flux and the number of muons becomes

$$\Phi(E_{\text{cut}}) = \frac{N_{\mu}}{\Delta A * \Delta T * \Delta \Omega} \quad (\text{E1})$$

One may also think of the number of recorded muons as the integral of the (integrated) flux over the detector area, the total exposure time and the covered solid angle. Eq. (E1) is consequently the reduced formulation if the integrated flux does not depend on the experimental parameters ΔA , ΔT or $\Delta \Omega$. In contrast to the detector size where this is generally the case, the exposure time may be an integral over seasonal variations. However, if the experiment is short enough or if the seasonal variations are small in the energy range one is looking at, one is usually fine with this approximation. The solid angle on the other hand could potentially introduce a large bias if unaccounted for (the muon flux depends strongly on the zenith angle). One remedy to this problem is the introduction of small bins that do not cover a large zenith angle interval.

If we can assume that the errors on ΔA , ΔT & $\Delta \Omega$ are well controllable and are thus negligible, the only real source of uncertainty is given by the counting statistics of N_{μ} . This can very well be modelled by a Poisson distribution, yielding a statistical error of

$$\varepsilon_N = \sqrt{\Phi * \Delta A * \Delta T * \Delta \Omega} \quad (\text{E2})$$

or

$$\epsilon_N = \sqrt{\Phi^* \Delta EXP} \quad (\text{E3})$$

where $\Delta EXP = \Delta A * \Delta T * \Delta \Omega$, is defined to be the ‘‘exposure’’. Performing a (Gaussian) uncertainty propagation on the equation $\Phi = N_\mu / \Delta EXP$ yields an absolute error of

$$\epsilon_\Phi = \sqrt{\frac{\Phi}{\Delta EXP}} \quad (\text{E4})$$

and a relative error of

$$\epsilon_\Phi = \frac{\epsilon_\Phi}{\Phi} = \sqrt{\frac{1}{\Phi^* \Delta EXP}} \quad (\text{E5})$$

respectively. Eq. (E5) can now be rearranged for the exposure,

$$\Delta EXP = \frac{1}{\Phi^* \epsilon_\Phi^2} \quad (\text{E6})$$

This formulation now allows for the calculation of the necessary exposure for a given flux and relative uncertainty. Recalling from Ch. 2.2.2 that the systematic error of the flux model is in the order of 15%, or 0.15, we may use this value for ϵ_Φ as we want the statistical error of the number of muons to be smaller or equal compared to the systematic flux error.

With help from the equations of Ch. 2 we compiled a graph (see Fig. E1) that shows how large the integrated muon flux after a certain thickness of rock is. Additionally, we put an equivalent graph next to it that converts the necessary exposure for a given rock thickness by using Eq. (E6) and $\epsilon_\Phi = 0.15$.

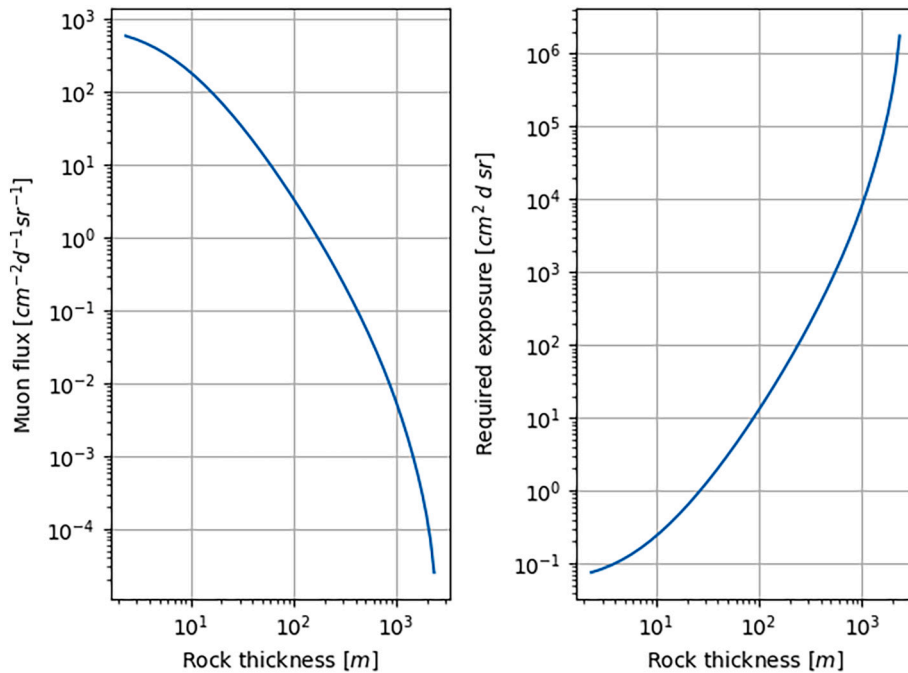


Fig. E1. *Left:* Integrated muon flux (Reyna-Bugaev model, see Appendix A1.2) as a function of rock thickness. *Right:* Required exposure to achieve a relative statistical error of 0.15 as a function of rock thickness (calculated with Eq. E6).

We can use this newly gained information on what amount of exposure we need to construct a function that may help us visualize which combinations of exposure parameters (i.e. detector area, exposure time and solid angle) are feasible. We proceed in writing the equation for the exposure in a slightly different way,

$$\Delta A = \frac{\Delta EXP}{\Delta T * \Delta \Omega} \quad (\text{E7})$$

At this point we make use of the fact that the solid angle is often rather small, as researchers tend to bin the measured muons in directional bins. In this way detailed directional information can be used for a much more precise tomography. The definition of the solid angle is given as the surface of the sphere at distance D within the bin margins divided by the radius of the sphere squared, D^2 . At large distances this spherical surface can be approximated by the tangential surface, whose area is much easier to compute, i.e. $\Delta X * \Delta Y$, where X and Y are the width and the height of the tangential surface. The solid angle can thus be approximately calculated by

$$\Delta \Omega \approx \frac{\Delta X * \Delta Y}{D^2} \quad (\text{E8})$$

For computational convenience we assume a quadratic bin, such that Eq. (E8) can be recast into

$$\Delta\Omega = \frac{\Delta Res^2}{D^2} \tag{E9}$$

where we substituted ΔX and ΔY each with ΔRes , the lateral resolution in a distance unit (usually metres).

Putting Eq. (E9) into Eq. (E7) gives

$$\Delta A = \frac{\Delta Exp * D^2}{\Delta T * \Delta Res^2} \tag{E10}$$

This equation can be put in an even simpler form by taking the logarithm on both sides,

$$\log(\Delta A) = -\log(\Delta T) + \log\left(\frac{\Delta Exp * D^2}{\Delta Res^2}\right) \tag{E11}$$

Eq. (E11) is a linear equation on a Log-Log plot where the exposure time is on the x-axis and the detector size is on the y-axis. For a given rock thickness, D , also the exposure is fixed (see Fig. E1), this making the lateral spatial resolution, ΔRes , the last variable that has to be chosen. A summary for different rock thicknesses can be seen in Fig. E2.

For computational simplicity, we display the detector size axis in two different colours indicating two different measurement units that are often used to describe the detector area. One sees also nicely that the variation of the lateral spatial resolution affects the linear relationship only as an offset.

A recipe and an example on how to choose valid exposure parameters can be found in Ch. 4.2.

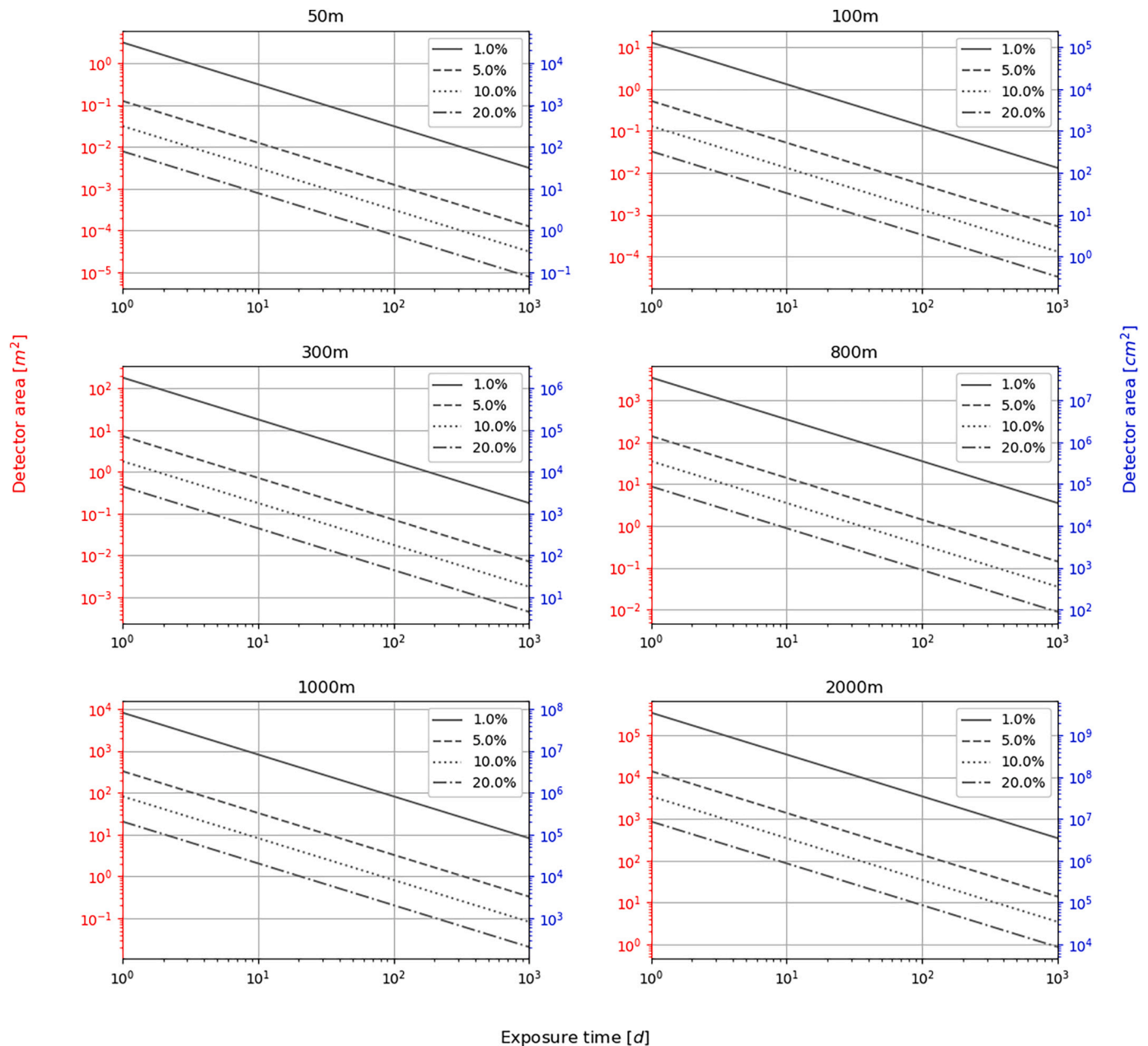


Fig. E2. Decision help chart for the two experimental parameters, which are detector size and exposure time for various rock thicknesses. Parallel lines indicate the amount of desired lateral precision one can achieve by using a corresponding area/time-point.

References

- Acquafredda, R., et al., 2009. The OPERA experiment in the CERN to Gran Sasso neutrino beam. *J. Instrum.* 4 <https://doi.org/10.1088/1748-0221/4/04/P04018>.
- Agostinelli, S., et al., 2003. Geant4—a simulation toolkit. In: *Nuclear Instruments and Methods in Physics Research Section a: Accelerators, Spectrometers, Detectors and Associated Equipment*, 506, pp. 250–303. [https://doi.org/10.1016/S0168-9002\(03\)01368-8](https://doi.org/10.1016/S0168-9002(03)01368-8).
- Aitchison, J., 1986. *The Statistical Analysis of Compositional Data*. Chapman and Hall Ltd, New York.
- Alvarez, L.W., Anderson, J.A., El Bedwei, F., Burkhard, J., Fakhry, A., Girgis, A., Goneid, A., Hassan, F., Iverson, D., Lynch, G., Miligy, Z., Moussa, A.H., Mohammed-Sharkawi, Yazolino, L., 1970. Search for hidden chambers in the pyramids. *Science* 167, 832–839.
- Ambrosino, F., Anastasio, A., Bross, A., Béné, S., Boivin, P., Bonechi, L., Cârloganu, C., Ciaranfi, R., Cimmino, L., Combaret, C., D'Alessandro, R., Durand, S., Fehr, F., François, V., Garufi, F., Gailler, L., Labazuy, P., Laktineh, I., Lénat, J.-F., Masone, V., Miallier, D., Mirabito, L., Morel, L., Mori, N., Niess, V., Noli, P., Pla-Dalmau, A., Portal, A., Rubinov, P., Saracino, G., Scarlini, E., Strolin, P., Vulpesu, B., 2015. Joint measurement of the atmospheric muon flux through the Puy de Dôme volcano with plastic scintillators and Resistive Plate Chambers detectors. *J. Geophys. Res. Solid Earth* 120, 7290–7307. <https://doi.org/10.1002/2015JB011969>.
- Anderson, C.D., 1932. The apparent existence of easily deflectable positives. *Science* 76, 238–239. <https://doi.org/10.1126/science.76.1967.238>.
- Ariga, A., Ariga, T., Ereditato, A., Käser, S., Lechmann, A., Mair, D., Nishiyama, R., Pistillo, C., Scampoli, P., Schlunegger, F., Vladymyrov, M., 2018. A nuclear emulsion detector for the Muon radiography of a glacier structure. *Instruments* 2, 7. <https://doi.org/10.3390/instruments2020007>.
- Athanassas, C.D., 2020. Muography for geological hazard assessment in the South Aegean active volcanic arc (SAAVA). *Med. Geosci. Rev.* <https://doi.org/10.1007/s42990-020-00020-x>.
- Baccani, G., Bonechi, L., Bonghi, M., Brocchini, D., Casagli, N., Ciaranfi, R., Cimmino, L., Ciulli, V., D'Alessandro, R., Del Ventisette, C., Dini, A., Gigli, G., Gonzi, S., Guideri, S., Lombardi, L., Melon, B., Mori, N., Nocentini, M., Noli, P., Saracino, G., Viliani, L., 2019. Muon Radiography of Ancient Mines: the San Silvestro Archaeo-mining Park (Campiglia Marittima, Tuscany), *Universe*, 5, p. 34. <https://doi.org/10.3390/universe5010034>.
- Barnaöföldi, G.G., Hamar, G., Melegh, H.G., Oláh, L., Surányi, G., Varga, D., 2012. Portable cosmic muon telescope for environmental applications. In: *Nuclear Instruments and Methods in Physics Research Section a: Accelerators, Spectrometers, Detectors and Associated Equipment*, 689, pp. 60–69. <https://doi.org/10.1016/j.nima.2012.06.015>.
- Barnoud, A., Cayol, V., Niess, V., Cârloganu, C., Lelièvre, P., Labazuy, P., Le Ménédeu, E., 2019. Bayesian joint muographic and gravimetric inversion applied to volcanoes. *Geophys. J. Int.* 218, 2179–2194. <https://doi.org/10.1093/gji/ggz300>.
- Bettini, A., 2014a. *Introduction to Elementary Particle Physics, Second edition*. Cambridge University Press, New York.
- Bettini, A., 2014b. New underground laboratories: Europe, Asia and the Americas. *Phys. Dark Univ.* 4, 36–40. <https://doi.org/10.1016/j.dark.2014.05.006>.
- Bohr, N., 1913. On the constitution of atoms and molecules. *Philos. Mag.* 26, 1–25.
- Bonechi, L., D'Alessandro, R., Giammanco, A., 2020. Atmospheric muons as an imaging tool. *Rev. Phys.* 5, 100038. <https://doi.org/10.1016/j.revip.2020.100038>.
- Bonneville, A., Kouzes, R., Yamaoka, J., Lintereur, A., Flygare, J., Varner, G.S., Mostafanezhad, I., Guardincerri, E., Rowe, C., Mellors, R., 2019. Borehole muography of subsurface reservoirs. *Philos. Trans. R. Soc. A Math. Phys. Eng. Sci.* 377, 20180060. <https://doi.org/10.1098/rsta.2018.0060>.
- Bryman, D., Bueno, J., Davis, K., Kaminski, V., Liu, Z., Oldenburg, D., Pilkington, M., Sawyer, R., 2014. Muon geotomography - bringing new physics to orebody imaging. In: Kelley, K.D., Golden, H.C. (Eds.), *Building Exploration Capability for the 21st Century*. Society of Economic Geologists, Inc, Littleton, pp. 235–241.
- Bugaev, E.V., Misaki, A., Naumov, V.A., Sinegovskaya, T.S., Sinegovsky, S.I., Takahashi, N., 1998. Atmospheric Muon Flux at Sea Level, underground, and underwater. *Phys. Rev. D* 58, 054001. <https://doi.org/10.1103/PhysRevD.58.054001>.
- Caffau, E., Coren, F., Giannini, G., 1997. Underground cosmic-ray measurement for morphological reconstruction of the “Grotta Gigante” natural cave. In: *Nuclear Instruments and Methods in Physics Research Section a: Accelerators, Spectrometers, Detectors and Associated Equipment*, 385, pp. 480–488. [https://doi.org/10.1016/S0168-9002\(96\)01041-8](https://doi.org/10.1016/S0168-9002(96)01041-8).
- Catalano, O., Del Santo, M., Mineo, T., Cusumano, G., Maccarone, M.C., Pareschi, G., 2016. Volcanoes muon imaging using Cherenkov telescopes. In: *Nuclear Instruments and Methods in Physics Research Section a: Accelerators, Spectrometers, Detectors and Associated Equipment*, 807, pp. 5–12. <https://doi.org/10.1016/j.nima.2015.10.065>.
- Chadwick, J., 1932. The existence of a neutron. *Proc. R. Soc. Lond. A* 136, 692–708. <https://doi.org/10.1098/rspa.1932.0112>.
- de Asmundis, R., Avella, P., Toglia, F., 2007. Using RPC detectors as cosmic rays monitor. *IEEE Trans. Nucl. Sci.* 54, 670–676. <https://doi.org/10.1109/TNS.2007.895505>.
- Gaisser, T.K., Engel, R., Resconi, E., 2016. *Cosmic Rays and Particle Physics, Second edition*. Cambridge University Press, Cambridge.
- George, E., 1955. Cosmic rays measure overburden of tunnel. *Commonw. Eng.* 455–457.
- Gibert, D., Beauducel, F., Déclais, Y., Lesparre, N., Marteau, J., Nicollin, F., Tarantola, A., 2010. Muon tomography: plans for observations in the Lesser Antilles. *Earth Planet Sp.* 62, 153–165. <https://doi.org/10.5047/eps.2009.07.003>.
- Giomataris, Y., Rebourgeard, Ph., Robert, J.P., Charpak, G., 1996. MICROMEAS: a high-granularity position-sensitive gaseous detector for high particle-flux environments. In: *Nuclear Instruments and Methods in Physics Research Section a: Accelerators, Spectrometers, Detectors and Associated Equipment*, 376, pp. 29–35. [https://doi.org/10.1016/0168-9002\(96\)00175-1](https://doi.org/10.1016/0168-9002(96)00175-1).
- Gosse, J.C., Phillips, F.M., 2001. Terrestrial in situ cosmogenic nuclides: theory and application. *Quat. Sci. Rev.* 20, 1475–1560. [https://doi.org/10.1016/S0277-3791\(00\)00171-2](https://doi.org/10.1016/S0277-3791(00)00171-2).
- Groom, D.E., Mokhov, N.V., Striganov, S.I., 2001. Muon stopping power and range tables 10 MeV–100 TeV. *At. Data Nucl. Data Tables* 78, 183–356. <https://doi.org/10.1006/andn.2001.0861>.
- Harel, A., Yaish, D., 2019. Lingacom muography. *Philos. Trans. Royal Soc. A* 377, 20180133. <https://doi.org/10.1098/rsta.2018.0133>.
- Hebbeker, T., Timmermans, C., 2002. A compilation of high energy atmospheric muon data at sea level. *Astropart. Phys.* 18, 107–127. [https://doi.org/10.1016/S0927-6505\(01\)00180-3](https://doi.org/10.1016/S0927-6505(01)00180-3).
- Heck, D., Knapp, J., Capdevielle, J.N., Schatz, G., Thouw, T., 1998. CORSIKA: A Monte Carlo Code to Simulate Extensive Air Showers. *Forschungszentrum Karlsruhe GmbH, Karlsruhe*.
- Hess, V.F., 1912. Über Beobachtungen der Durchdringenden Strahlung Bei Sieben Freiballonfahrten, *Physikalische Z.* 13, pp. 1084–1091.
- Jourde, K., Gibert, D., Marteau, M., de Bremond d'Ars, J., Gardien, S., Girerd, C., Ianigro, J.-C., Carbone, D., 2013. Experimental detection of upward going cosmic particles and consequences for correction of density radiography of volcanoes. *Geophys. Res. Lett.* 40, 6334–6339. <https://doi.org/10.1002/2013GL058357>.
- Jourde, K., Gibert, D., Marteau, M., de Bremond d'Ars, J., Gardien, S., Girerd, C., Ianigro, J.-C., 2016. Monitoring temporal opacity fluctuations of large structures with muon radiography: a calibration experiment using a water tower. *Sci. Rep.* 6, 23054. <https://doi.org/10.1038/srep23054>.
- Kaiser, R., 2019. Muography: overview and future directions. *Philos. Trans. Royal Soc.* 377, 20180049. <https://doi.org/10.1098/rsta.2018.0049>.
- Kajita, T., Koshiba, M., Suzuki, A., 2012. On the origin of the Kamiokande experiment and neutrino astrophysics. *EPJ H* 37, 33–73. <https://doi.org/10.1140/epjh/e2012-30007-y>.
- Kearey, P., Brooks, M., Hill, I., 2002. *An Introduction to Geophysical Exploration, 3rd ed.* Blackwell Science, Malden, MA.
- Kirkpatrick, S., Gelatt, C.D., Vecchi, M.P., 1983. Optimization by simulated annealing. *Science* 220, 671–680. <https://doi.org/10.1126/science.220.4598.671>.
- Lechmann, A., 2021. *An Integrated Geological-Geophysical Approach to Subsurface Interface Reconstruction of Muon Tomography Measurements in High Alpine Regions*, PhD Thesis. University of Bern, Bern.
- Lechmann, A., Mair, D., Ariga, T., Ereditato, A., Nishiyama, R., Pistillo, C., Scampoli, P., Schlunegger, F., Vladymyrov, M., 2018. The effect of rock composition on muon tomography measurements. *Solid Earth* 9, 1517–1533. <https://doi.org/10.5194/se-9-1517-2018>.
- Lelièvre, P.G., Barnoud, A., Niess, V., Cârloganu, C., Cayol, V., Farquharson, C.G., 2019. Joint inversion methods with relative density offset correction for muon tomography and gravity data, with application to volcano imaging. *Geophys. J. Int.* 218, 1685–1701. <https://doi.org/10.1093/gji/ggz251>.
- Lesparre, N., Gibert, D., Marteau, J., Déclais, Y., Carbone, D., Galichet, E., 2010. Geophysical muon imaging: feasibility and limits. *Geophys. J. Int.* 183, 1348–1361. <https://doi.org/10.1111/j.1365-246X.2010.04790.x>.
- Lesparre, N., Gibert, D., Marteau, J., Komorowski, J.-C., Nicollin, F., Coutant, O., 2012. Density muon radiography of La Soufrière de Guadeloupe volcano: comparison with geological, electrical resistivity and gravity data. *Geophys. J. Int.* 190, 1008–1019. <https://doi.org/10.1111/j.1365-246X.2012.05546.x>.
- Lesparre, N., Cabrera, J., Marteau, J., 2017. 3-D density imaging with muon flux measurements from underground galleries. *Geophys. J. Int.* 208, 1579–1591. <https://doi.org/10.1093/gji/ggw482>.
- Lo Presti, D., Riggi, F., Ferlito, C., Bonanno, D.L., Bonanno, G., Gallo, G., La Rocca, P., Reito, S., Romeo, G., 2020. Muographic monitoring of the volcano-tectonic evolution of Mount Etna. *Sci. Rep.* 10, 11351. <https://doi.org/10.1038/s41598-020-68435-y>.
- Lynch, G.R., Dahl, O.L., 1991. Approximations to multiple Coulomb scattering. *Nucl. Instrum. Methods Phys. Res., Sect. B* 58, 6–10. [https://doi.org/10.1016/0168-583X\(91\)95671-Y](https://doi.org/10.1016/0168-583X(91)95671-Y).
- Marteau, J., Gibert, D., Lesparre, N., Nicollin, F., Noli, P., Giacoppo, F., 2012. Muons tomography applied to geosciences and volcanology. In: *Nuclear Instruments and Methods in Physics Research Section a: Accelerators, Spectrometers, Detectors and Associated Equipment*, 695, pp. 23–28. <https://doi.org/10.1016/j.nima.2011.11.061>.
- Maurer, H., Curtis, A., Boerner, D.E., 2010. Recent advances in optimized geophysical survey design. *GEOPHYSICS* 75, 75A177–75A194. <https://doi.org/10.1190/1.3484194>.
- McDonough, W.F., Šrámek, O., Wipperfurth, S.A., 2020. Radiogenic power and geoneutrino luminosity of the earth and other terrestrial bodies through time. *Geochem. Geophys. Geosyst.* 21 <https://doi.org/10.1029/2019GC008865> e2019GC008865.
- Morishima, K., Nishio, A., Moto, M., Nakano, T., Nakamura, M., 2017. Development of nuclear emulsion for muography. *Ann. Geophys.* 60, 0112. <https://doi.org/10.4401/ag-7387>.
- Nagahara, S., Miyamoto, S., 2018. Feasibility of three-dimensional density tomography using dozens of muon radiographies and filtered back projection for volcanoes. *Geosci. Instrum. Methods Data Syst.* 7, 307–316. <https://doi.org/10.5194/gi-7-307-2018>.

- Nagamine, K., 1995. Geo-tomographic observation of inner-structure of Volcano with Cosmic-ray Muons. *J. Geogr.* 104, 998–1007. <https://doi.org/10.5026/jgeography.104.7.998>.
- Nagamine, K., Iwasaki, M., Shimomura, K., Ishida, K., 1995. Method of probing inner-structure of geophysical substance with the horizontal cosmic-ray muons and possible application to volcanic eruption prediction. In: *Nuclear Instruments and Methods in Physics Research Section a: Accelerators, Spectrometers, Detectors and Associated Equipment*, 356, pp. 585–595. [https://doi.org/10.1016/0168-9002\(94\)01169-9](https://doi.org/10.1016/0168-9002(94)01169-9).
- Neddermeyer, S.H., Anderson, C.D., 1937. Note on the nature of cosmic-ray particles. *Phys. Rev.* 51, 884–886.
- Niess, V., Barnoud, A., Cârloganu, C., Le Ménède, E., 2018. Backward Monte-Carlo applied to muon transport. *Comput. Phys. Commun.* 229, 54–67. <https://doi.org/10.1016/j.cpc.2018.04.001>.
- Nishiyama, R., Tanaka, Y., Okubo, S., Oshima, H., Tanaka, H.K.M., Maekawa, T., 2014. Integrated processing of muon radiography and gravity anomaly data toward the realization of high-resolution 3-D density structural analysis of volcanoes: Case study of Showa-Shinzan lava dome, Usu, Japan. *J. Geophys. Res. Solid Earth* 119, 699–710. <https://doi.org/10.1002/2013JB010234>.
- Nishiyama, R., Miyamoto, S., Naganawa, N., 2015. Application of emulsion cloud chamber to cosmic-ray muon radiography. *Radiat. Meas.* 83, 56–58. <https://doi.org/10.1016/j.radmeas.2015.04.013>.
- Nishiyama, R., Ariga, A., Ariga, T., Käser, S., Lechmann, A., Mair, D., Scampoli, P., Vladymyrov, M., Ereditato, A., Schlunegger, F., 2017. First measurement of ice-bedrock interface of alpine glaciers by cosmic muon radiography. *Geophys. Res. Lett.* 44, 6244–6251. <https://doi.org/10.1002/2017GL073599>.
- Nishiyama, R., Ariga, A., Ariga, T., Lechmann, A., Mair, D., Pistillo, C., Scampoli, P., Valla, P.G., Vladymyrov, M., Ereditato, A., Schlunegger, F., 2019. Bedrock sculpting under an active alpine glacier revealed from cosmic-ray muon radiography. *Sci. Rep.* 9, 6970. <https://doi.org/10.1038/s41598-019-43527-6>.
- Oláh, L., Barnaföldi, G.G., Hamar, G., Melegh, H.G., Surányi, G., Varga, D., 2012. CCC-based muon telescope for examination of natural caves. *Geosci. Instrum. Method. Data Syst.* 1, 229–234. <https://doi.org/10.5194/gi-1-229-2012>.
- Oláh, L., Hamar, G., Miyamoto, S., Tanaka, H.K.M., Varga, D., 2018. The First Prototype of an MWPC-Based Borehole-Detector and its Application for Muography of an Underground Pillar, BUTSURI-TANSA(Geophysical Exploration), 71, pp. 161–168. <https://doi.org/10.3124/segi.71.161>.
- Oláh, L., Tanaka, H.K.M., Ohminato, T., Hamar, G., Varga, D., 2019. Plug formation imaged beneath the active craters of Sakurajima Volcano with muography. *Geophys. Res. Lett.* 46, 10417–10424. <https://doi.org/10.1029/2019GL084784>.
- Pacini, D., 1912. La radiazione penetrante alla superficie ed in seno alle acque. *Il Nuovo Cimento* 3, 93–100.
- Pla-Dalmau, A., Bross, A.D., Mellott, K.L., 2001. Low-cost extruded plastic scintillator. In: *Nuclear Instruments and Methods in Physics Research Section a: Accelerators, Spectrometers, Detectors and Associated Equipment*, 466, pp. 482–491. [https://doi.org/10.1016/S0168-9002\(01\)00177-2](https://doi.org/10.1016/S0168-9002(01)00177-2).
- Procureur, S., 2018. Muon imaging: Principles, technologies and applications. In: *Nuclear Instruments and Methods in Physics Research Section a: Accelerators, Spectrometers, Detectors and Associated Equipment*, 878, pp. 169–179. <https://doi.org/10.1016/j.nima.2017.08.004>.
- Reichstein, M., Camps-Valls, G., Stevens, B., Jung, M., Denzler, J., Carvalhais, N., 2019. and Prabhat: deep learning and process understanding for data-driven Earth system science. *Nature* 566, 195–204. <https://doi.org/10.1038/s41586-019-0912-1>.
- Reyna, D., 2006. A simple parameterization of the Cosmic-Ray Muon momentum spectra at the surface as a function of Zenith angle. *arXiv Prepr. (hep-ph/0604145 [online] Available from: http://arxiv.org/abs/hep-ph/0604145)*.
- Rosas-Carbajal, M., Jourde, K., Marteau, J., Deroussi, S., Komorowski, J.-C., Gibert, D., 2017. Three-dimensional density structure of La Soufrière de Guadeloupe lava dome from simultaneous muon radiographies and gravity data. *Geophys. Res. Lett.* 44, 6743–6751. <https://doi.org/10.1002/2017GL074285>.
- Rücker, C., Günther, T., Wagner, F.M., 2017. pyGIMLi: an open-source library for modelling and inversion in geophysics. *Comput. Geosci.* 109, 106–123. <https://doi.org/10.1016/j.cageo.2017.07.011>.
- Rutherford, E., 1911. LXXIX. The scattering of α and β particles by matter and the structure of the atom. *Lond. Edinb. Dublin Philos. Mag. J. Sci.* 21, 669–688. <https://doi.org/10.1080/14786440508637080>.
- Rutherford, E., 1919. LIV. Collision of α Particles with Light Atoms. IV. An Anomalous Effect in Nitrogen, 37, pp. 31–37. <https://doi.org/10.1080/14786440608635919>.
- Sato, T., 2016. Analytical model for estimating the zenith angle dependence of terrestrial cosmic ray fluxes. *PLoS One* 11, e0160390. <https://doi.org/10.1371/journal.pone.0160390>.
- Sato, T., Niita, K., Matsuda, N., Hashimoto, S., Iwamoto, Y., Noda, S., Ogawa, T., Iwase, H., Nakashima, H., Fukahori, T., Okumura, K., Kai, T., Chiba, S., Furuta, T., Sihver, L., 2013. Particle and heavy ion transport code system, PHITS, version 2.52. *J. Nucl. Sci. Technol.* 50, 913–923. <https://doi.org/10.1080/00223131.2013.814553>.
- Schwarz, S., 2013. Validation of Geant4 Proton Scattering A Summer Student Project. CERN, Geneva.
- Sivia, D.S., Skilling, J.H., 2012. *Data Analysis: A Bayesian Tutorial, Second edition*. Oxford Univ. Press, Oxford.
- Šrámek, O., McDonough, W.F., Kite, E.S., Lekić, V., Dye, S.T., Zhong, S., 2013. Geophysical and geochemical constraints on geoneutrino fluxes from Earth's mantle. *Earth Planet. Sci. Lett.* 361, 356–366. <https://doi.org/10.1016/j.epsl.2012.11.001>.
- Stoer, J., Bulirsch, R., 2013. *Introduction to Numerical Analysis*. Springer Science & Business Media, New York.
- Tanabashi, M., et al., 2018. (Particle data group): review of particle physics. *Phys. Rev. D* 98, 030001. <https://doi.org/10.1103/PhysRevD.98.030001>.
- Tanaka, H.K.M., Oláh, L., 2019. Overview of muographers. *Philos. Trans. R. Soc. A Math. Phys. Eng. Sci.* 377, 20180143. <https://doi.org/10.1098/rsta.2018.0143>.
- Tanaka, H., Nagamine, K., Kawamura, N., Nakamura, S.N., Ishida, K., Shimomura, K., 2001. Development of the cosmic-ray muon detection system for probing internal-structure of a Volcano. *Hyperfine Interactions* 138, 521–526. <https://doi.org/10.1023/A:1020843100008>.
- Tanaka, H., Nagamine, K., Kawamura, N., Nakamura, S.N., Ishida, K., Shimomura, K., 2003. Development of a two-fold segmented detection system for near horizontally cosmic-ray muons to probe the internal structure of a volcano. In: *Nuclear Instruments and Methods in Physics Research Section a: Accelerators, Spectrometers, Detectors and Associated Equipment*, 507, pp. 657–669. [https://doi.org/10.1016/S0168-9002\(03\)01372-X](https://doi.org/10.1016/S0168-9002(03)01372-X).
- Tanaka, H.K.M., Nagamine, K., Nakamura, S.N., Ishida, K., 2005. Radiographic measurements of the internal structure of Mt. West Iwate with near-horizontal cosmic-ray muons and future developments. In: *Nuclear Instruments and Methods in Physics Research Section a: Accelerators, Spectrometers, Detectors and Associated Equipment*, 555, pp. 164–172. <https://doi.org/10.1016/j.nima.2005.08.099>.
- Tanaka, H.K.M., Nakano, T., Takahashi, S., Yoshida, J., Takeo, M., Oikawa, J., Ohminato, T., Aoki, Y., Koyama, E., Tsuji, H., Niwa, K., 2007. High resolution imaging in the inhomogeneous crust with cosmic-ray muon radiography: the density structure below the volcanic crater floor of Mt. Asama, Japan. *Earth Planet. Sci. Lett.* 263, 104–113. <https://doi.org/10.1016/j.epsl.2007.09.001>.
- Tanaka, H.K.M., Uchida, T., Tanaka, M., Shinohara, H., Taira, H., 2009. Cosmic-ray muon imaging of magma in a conduit: Degassing process of Satsuma-Iwojima Volcano, Japan. *Geophys. Res. Lett.* 36. <https://doi.org/10.1029/2008GL036451>.
- Tanaka, H.K.M., Miyajima, H., Kusagaya, T., Taketa, A., Uchida, T., Tanaka, M., 2011. Cosmic muon imaging of hidden seismic fault zones: Rainwater permeation into the mechanical fractured zones in Itoigawa-Shizuoka Tectonic Line, Japan. *Earth Planet. Sci. Lett.* 306, 156–162. <https://doi.org/10.1016/j.epsl.2011.03.036>.
- Tanaka, H.K.M., Kusagaya, T., Shinohara, H., 2014. Radiographic visualization of magma dynamics in an erupting volcano. *Nat. Commun.* 5, 3381. <https://doi.org/10.1038/ncomms4381>.
- Tang, A., Horton-Smith, G., Kudryavtsev, V.A., Tonazzo, A., 2006. Muon simulations for super-Kamiokande, KamLAND and CHOOZ. *Phys. Rev. D* 74, 053007. <https://doi.org/10.1103/PhysRevD.74.053007>.
- Tarantola, A., 2005. *Inverse Problem Theory and Methods for Model Parameter Estimation, 1st ed., Siam, Philadelphia*.
- Tioukov, V., Alexandrov, A., Bozza, C., Consiglio, L., D'Ambrosio, N., De Lellis, G., De Sio, C., Giudicepietro, F., Macedonio, G., Miyamoto, S., Nishiyama, R., Orazi, M., Peluso, R., Sheshukov, A., Sirignano, C., Stellacci, S.M., Strolin, P., Tanaka, H.K.M., 2019. First muography of Stromboli volcano. *Sci. Rep.* 9, 6695. <https://doi.org/10.1038/s41598-019-43131-8>.
- Tsai, Y.-S., 1974. Pair production and bremsstrahlung of charged leptons. *Rev. Mod. Phys.* 46, 815–851. <https://doi.org/10.1103/RevModPhys.46.815>.
- Varga, D., Nyitrai, G., Hamar, G., Oláh, L., 2016. High efficiency gaseous tracking detector for cosmic muon radiography. *Adv. High Energy Phys.* 1–11. <https://doi.org/10.1155/2016/1962317>. Article ID 1962317.
- Varga, D., Nyitrai, G., Hamar, G., Galgóczi, G., Oláh, L., Tanaka, H.K.M., Ohminato, T., 2020. Detector developments for high performance Muography applications. In: *Nuclear Instruments and Methods in Physics Research Section A: Accelerators, Spectrometers, Detectors and Associated Equipment*, 958, p. 162236. <https://doi.org/10.1016/j.nima.2019.05.077>.
- Vesga-Ramírez, A., Sanabria-Gómez, J.D., Sierra-Porta, D., Arana-Salinas, L., Asorey, H., Kudryavtsev, V.A., Calderón-Ardila, R., Núñez, L.A., 2021. Simulated Annealing for volcano muography. *J. S. Am. Earth Sci.* 109, 103248. <https://doi.org/10.1016/j.jsames.2021.103248>.
- Wulf, T., 1910. About the radiation of high penetration capacity contained in the atmosphere. *Phys. Z.* 5, 152–157.